Journal of Volcanology and Geothermal Research 272 (2014) 111–125

Contents lists available at ScienceDirect

Journal of Volcanology and Geothermal Research

journal homepage: www.elsevier.com/locate/jvolgeores

Large-scale catastrophic flank collapses in a steep volcanic ridge: The Pico–Faial Ridge, Azores Triple Junction

A.C.G. Costa [a,b,c,d,*], F.O. Marques [a], A. Hildenbrand [c,d], A.L.R. Sibrant [c,d], C.M.S. Catita [a,b]

[a] University of Lisbon, Lisbon, Portugal
[b] IDL, Lisbon, Portugal
[c] Univ. Paris-Sud, Laboratoire IDES, UMR8148, Orsay F-91405, France
[d] CNRS, Orsay F-91405, France

ARTICLE INFO

Article history:
Received 16 September 2013
Accepted 6 January 2014
Available online 17 January 2014

Keywords:
Large-scale flank collapse
Debris deposit
Steep volcanic ridge
Mass wasting
Pico Island
Azores

ABSTRACT

Large-scale flank collapses are common in the geological evolution of volcanic ocean islands in the Atlantic. To date, catastrophic lateral collapses in the Azores Islands have been difficult to identify, leading to suggestions that a lack of events may relate to the relatively small size of the islands. Here we show evidence for two major collapses on the northern flank of Pico Island (Pico–Faial volcanic ridge, central Azores), suggesting that this island had a collapse incidence similar to that of other Atlantic volcanic islands.

The study is based on the analysis of: (1) offshore and onshore high-resolution digital elevation models; (2) field data focused on the N flank; and (3) new K–Ar ages on selected lava flow samples.

Pico sub-aerial northern flank is marked by two conspicuous arcuate shaped depressions concave towards the sea, here interpreted as landslide scars. A main debris field is observed offshore the largest depression. This deposit has 20 km of maximum length, covers ca. 150 km^2, is composed of meter to hectometer blocks, and has an exposed volume here estimated between 4 and 10 km^3, though the actual volume probably exceeds 10 km^3. Debris flow towards the ESE was apparently determined by the slope of the narrow WNW–ESE S. Jorge channel.

Young lava flows cascade over the interpreted scars, thus concealing the older volcanic sequence(s) affected by the landslide(s). New K–Ar ages measured on these lava flows provide a minimum age of ca. 70 ka for the large-scale collapse(s) in Pico's northern flank.

1. Introduction

The destruction of volcanic islands occurs at small and large scales, gradually or suddenly on catastrophic events. Large-scale flank failure in volcanic islands can involve either gradual movement along deep listric faults (slump) or the generation of debris avalanche (Moore et al., 1989). These two mechanisms are not mutually exclusive, as a creeping slump may suddenly turn into a catastrophic debris avalanche. From on-land and offshore studies, catastrophic large-scale mass wasting has been identified on volcanic islands all over the world (e.g., Duffield et al., 1982; Moore et al., 1989; Gillot et al., 1994; Deplus et al., 2001; Krastel et al., 2001; Masson et al., 2002; Hildenbrand et al., 2006). In the Atlantic, more specifically, catastrophic failure episodes have been extensively documented, e.g. in the Canary (Navarro and Coello, 1989; Carracedo et al., 1999; Krastel et al., 2001; Masson et al., 2002; Boulesteix et al., 2012, 2013), in Cape Verde (e.g., Day et al., 1999; Masson et al., 2008), and along the Caribbean arc (Deplus et al., 2001; Le Friant et al., 2003; Samper et al., 2007; Germa et al., 2011).

To date, catastrophic flank collapses in the Azores Islands have been difficult to identify, leading to suggestions that a lack of collapses may relate to the relatively small volume of individual islands and volcanic ridges (e.g. Mitchell, 2003). Two topographic embayments on the southern flank of Pico Island have been related to lateral flank movement in the form of old catastrophic landslides or slumping processes (Woodhall, 1974; Madeira, 1998; Nunes, 1999, 2002; Madeira and Brum da Silveira, 2003; Hildenbrand et al., 2012b, 2013b; Mitchell et al., 2012, 2013), but none of these features is clearly and unambiguously associated with well-identified offshore deposits.

Here we put forward evidence of two major collapses, and respective submarine deposits, on Pico's northern flank, showing that the island has experienced episodes of flank instability like other Atlantic volcanic islands.

The identification of offshore debris deposits and the interpretation of onshore source zones in Pico's northern flank are here primarily based on morphological characterization, through combined analysis of a 10 m resolution sub-aerial digital elevation model (DEM) and the new 50 m resolution bathymetry of the narrow S. Jorge Channel (between Pico's northern flank and S. Jorge's southern flank). The analysis of the bathymetry also supports the discussion of the influence of channel morphology on the landslide submarine flow and deposition.

* Corresponding author at: University of Lisbon and IDL, Lisbon, Portugal. Tel.: +351 918318361.
E-mail address: acgcosta@fc.ul.pt (A.C.G. Costa).

0377-0273/$ – see front matter © 2014 Elsevier B.V. All rights reserved.
http://dx.doi.org/10.1016/j.jvolgeores.2014.01.002

In order to determine the age and recurrence of the failure events, we performed fieldwork focused on the establishment of volcanic stratigraphy/structure of the source zones, aiming at finding possible landslide scars/deposits and to sample the volcanic sequences affected by and covering the landslide related features. The sampled rocks were then processed according to the K–Ar Cassignol–Gillot unspiked technique.

2. Geologic setting

The Azores Islands are located about the triple junction between North-America, Eurasia and Nubia plates (Fig. 1). The study region is located on the locally diffuse Nubia/Eurasia plate boundary (Lourenço et al., 1998; Fernandes et al., 2006; Borges et al., 2007; Marques et al., 2013), where regional deformation has influenced the development of narrow and steep volcanic ridges (Fig. 1). The volcanic ridges of S. Jorge and Pico–Faial (Fig. 1) are characterized by slopes commonly around 25–35°, locally reaching higher values along coastal cliffs. These ridges are characterized by a multi-stage development during the last 1.3 Myr (Féraud et al., 1980; Demande et al., 1982; Hildenbrand et al., 2008, 2012a). This multi-stage development includes short periods of volcanic construction interrupted by long periods of island destruction. The island destruction processes are either gradual (e.g., erosion, graben development) or catastrophic like the events here reported. The growth of the sub-aerial Pico–Faial ridge started ca. 850 ka ago on the eastern part of Faial Island (Quartau et al., 2010, 2012; Hildenbrand et al., 2012a, 2013a; Quartau and Mitchell, 2013), with the growth of sub-aerial Pico during the last ca. 300 ka (Fig. 2, 250 ± 40 ka, in Demande et al., 1982). The oldest outcropping volcanic unit in Pico, the Topo Unit (TU), is located on its SE flank (Fig. 2), which is deeply affected by a currently active slump structure (Hildenbrand et al., 2012b) (Fig. 3, feature 1). A WNW–ESE fissural system (FS) developed N of Topo (Fig. 2), and a stratovolcano (Fig. 2, PS) constitutes the westernmost part of the island (Fig. 2, e.g., Forjaz 1966); both have been volcanically active through the Holocene and in historic times (Madeira, 1998; Nunes, 1999; Mitchell et al., 2008). Two topographic embayments on Pico's northern flank (Fig. 3) were considered by Mitchell (2003) as "ambiguous candidates for landslides". Mitchell et al. (2008) identified a hummocky terrain area on the shallow bathymetry (depth up to of a few hundred meters) adjacent to a sub-aerial embayment (Fig. 2 in Mitchell et al., 2008, feature A), which was interpreted as a deposit resulting from debris avalanche or repeated lava delta failure. Despite these evidences, to date the published works (e.g., Mitchell, 2003; Mitchell et al., 2008) do not conclude unequivocally on the occurrence of major landslides in Azores islands.

3. Morphological analysis

3.1. Construction of the DEMs

The submarine grid of the deepest sector of the Pico–S. Jorge channel (50 m resolution, Fig. A.1a) was constructed using the multibeam data acquired with a 12 kHz Kongsberg EM120 multibeam echo sounder system (Lourenço, personal communication). The depth accuracy (RMS) for this system is estimated as 0.2–0.5% of the water depth (Kongsberg, 2007). Considering that the maximum water depth in the study area is ca. 1300 m, the maximum RMS expected for this data set lies in the range 2.6–6.5 m.

The multibeam data were processed using the CARIS software, clean of noise and converted to an ASCII file (Lourenço, personal communication). Next, the 50 m resolution ASCII data were converted to a raster structure of 50 m spatial resolution, using a simple gridding method.

The onshore data used in this study was produced from a digital topographic map of Pico Island (Portuguese Army Geographic Institute, IGeoE). Photogrammetric methods led to the production of this information at the 1:25,000 scale. The vertical accuracy of these data is approximately 5 m (Afonso et al., 2002). The nodes and lines with three-dimensional coordinates (x, y and z) of the contour lines were then used to generate a TIN (Triangulated Irregular Network) model, which is a vector-based representation of the relief based on a network of non-overlapping triangles (Burrough and McDonnell, 1998). The conversion of the TIN model to a raster structure was then performed interpolating the cell z-values from the input TIN at the spatial resolution of 10 m and 50 m to produce the final onshore DEMs for Pico Island (10 m spatial resolution), S. Jorge and Faial Islands (50 m spatial resolution). To this purpose, we used the ArcGIS 9.3 software from ESRI with the 3D Analyst extension. For the final grid, we introduced in the no-data zone on Pico's northern coast (between the sub-aerial and submarine grids described above) the 100 m spaced contours obtained from photogrammetry of Fig. 2 in Mitchell et al. (2008). The final 50 m resolution grid was built through combination of the sub-aerial and submarine DEMs described above (Fig. 4), filling the no-data zone with a 200 m resolution interpolation that included the depth contours

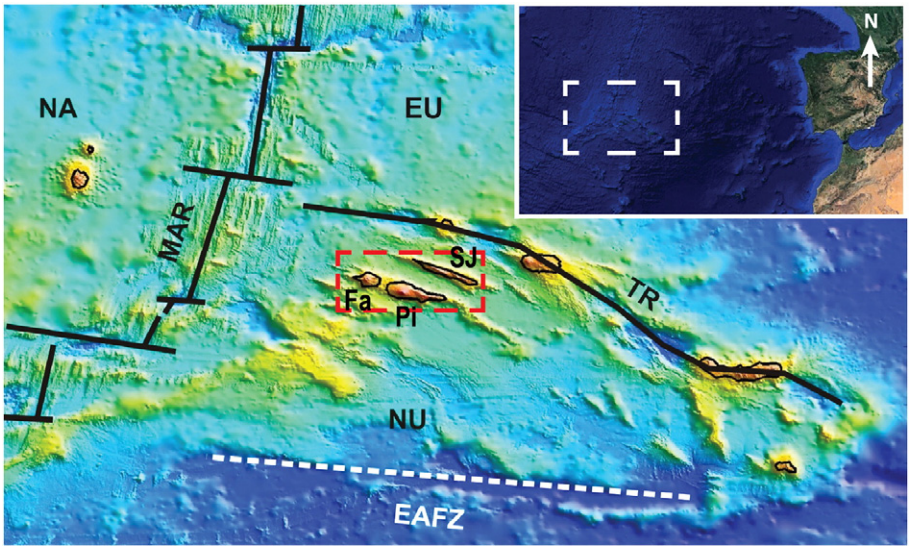

Fig. 1. Location of the Azores archipelago on the triple junction between the North America (NA), Eurasia (EU) and Nubia (NU) plates. Main active structures represented as thick black lines (Middle Atlantic Ridge — MAR, Terceira Rift — TR) and inactive structure as dashed white line (East Azores Fracture Zone — EAFZ). The white dashed rectangle encompassing the islands of Pico (Pi), S. Jorge (SJ) and Faial (Fa) limits the study area. Bathymetric data from Lourenço et al. (1998); Image available at http://w3.ualg.pt/~jluis/acores_plateau.htm. (right top rectangle) Inset for the location of the Azores Triple Junction (Google Earth image — 19-08-2013).

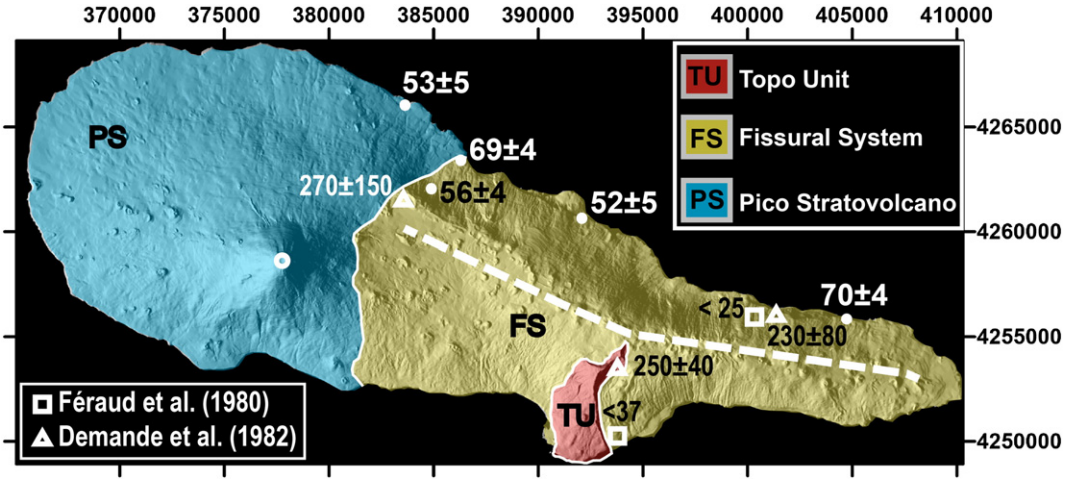

Fig. 2. Shaded relief of the 10 m resolution DEM of Pico Island (lighting from ESE), with coordinates in meters UTM (zone 26N). White dots and numbers along Pico's northern flank mark the location and the K–Ar ages presented in this study. White squares and triangles mark the K–Ar ages presented in Féraud et al. (1980) and Demande et al. (1982), respectively. The ages are indicated in thousands of years (ka). Simplified geologic/physiographic map (modified after Madeira, 1998).

extracted from Mitchell et al. (2008). Further details on the composition of the final DEM grid are provided in Appendix A.

For the construction of Pico's elevation gradient in the sub-aerial domain (Fig. 3), we took the original 10 m resolution elevation grid of the sub-aerial domain and created a final 10 m resolution terrain slope grid in the Surfer software (Golden Software, Inc.; software version 9.11.47). For each grid node, the angle of dip was calculated considering the elevation gradients between neighboring nodes in N–S and E–W directions (Golden Software, Inc., 2002, after Moore et al., 1993). Therefore, though the final slope grid presents values for 10 m spaced nodes, the calculation of the final values is based on the elevation gradient between nodes at a 20 m distance from each other (twice the horizontal resolution of the original DEM).

3.2. Pico's sub-aerial northern flank

On an elevation gradient map (Fig. 3), the northern flank is generally steeper than the southern flank. On the northern flank, the sub-aerial elevation gradient of the fissural system (Fig. 2, FS) reaches 30–45° on two sectors of concave profile, reaching ca. 800 m of maximum height (Fig. 3):

1. On the western sector of the fissural system, the 30–45° slopes are aligned WNW–ESE (Fig. 3, feature 2). They are masked in the west and in the east by more recent volcanic deposits erupted by the younger Pico stratovolcano and by the fissural system, respectively (Figs. 2 and 3).
2. On the eastern sector of the northern flank, the steep slopes define an arcuate topography, which is concave towards the sea and grossly parallel to the volcanic ridge axis (Fig. 3, feature 3).

3.3. S. Jorge Channel bathymetry

The building of the grid mosaic, combining sub-aerial and submarine grids, is described in Appendix A of the supplementary material.

Pico and S. Jorge islands are separated by a ca. 20 km wide WNW–ESE channel, known as the S. Jorge Channel (Fig. 4). The maximum depth along its axis varies between ca. −1230 m and −1270 m, with a basal surface defined around −1270 m, deepening towards its

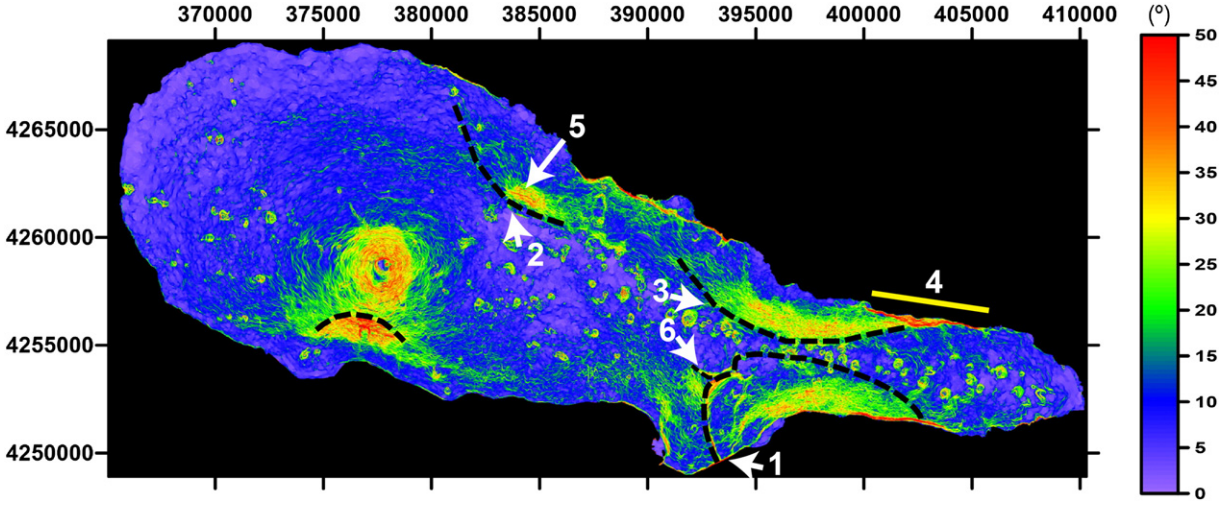

Fig. 3. Slope map of Pico Island built from the 10 m resolution DEM. Dashed black lines: scarps interpreted from zones of anomalously strong slopes. Numbered features: 1 — active slump; 2 — westernmost scar of Pico's N flank; 3 — easternmost scar of Pico's N flank coastal; 4 — coastal cliff mentioned in Section 4; 5 — location of the creeks referred to in Section 4; 6 — scarp that limits the outcropping TU to the N.

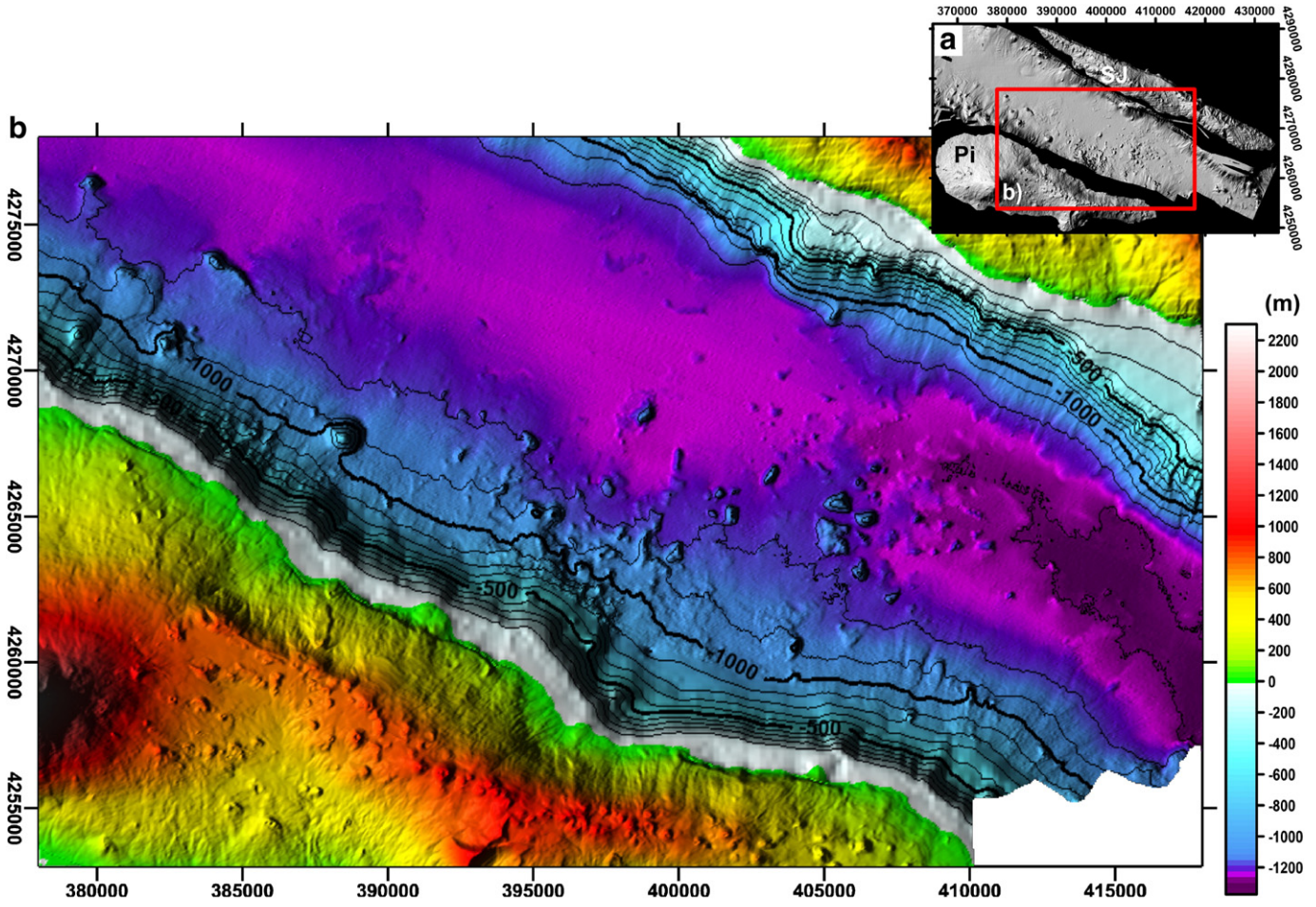

Fig. 4. Topographic grid used as basis for this study. (a) Shaded relief (50 m resolution, lighting from WNW) of Pico Island (Pi), S. Jorge Island (SJ) and bathymetry of S. Jorge channel. The red rectangle indicates the area comprised in b. (b) Final grid resulting from the combination of the DEMs presented in (a) and contours extracted from Mitchell et al. (2008) (50 m resolution, lighting from W). Contour levels for 100 m spaced depths are presented. A detailed description of the grid construction is presented in Appendix A.

WNW and ESE ends. On the bathymetry of the S. Jorge Channel (Fig. 5a), we identified:

1. The main feature in the central sector, a WSW–ENE elongated hummocky area, with a positive relief relative to the surrounding sea floor (Fig. 6a, feature "A"). It has a maximum visible length of 20 km (ca. 22 km, measured along a longitudinal profile) and spreads over an area of ca. 150 km^2. The grain size of the material at the surface of this positive-relief feature is generally too small to be distinguishable on this 50 m resolution DEM. The largest individual hummocks observed are located on the distal part of the deposit, at an average depth of −1240 m (Fig. 6a): the largest is 1700 m long, 1200 m wide and 100 m high (Fig. 6a, feature 1), and the second largest is 1000 m long, 600 m wide and 200 m high (Fig. 6a, feature 2). On the SE zone of the hummocky terrain, a homogeneous mass of, apparently, intermediate size debris material can be identified (Fig. 6a, feature "A", dashed yellow line). At the foot of Pico's submarine flank, on the surface of this homogeneous mass (high resolution bathymetry presented as Fig. 2 in Mitchell et al., 2008), there are visible lineaments perpendicular to the submarine flank. Uphill, on the submarine flank, there are two small arcuate scarps (Fig. 6a, red dashed lines).
2. A NNE–SSW elongated, lobate-shaped hummocky terrain on the western sector (Fig. 6a, feature "B"). Its maximum extent is ca. 8 km, measured from, and perpendicularly to, the base of Pico's submarine flank. It is generally composed of small debris, undistinguishable on the 50 m resolution DEM, but with some larger hummocks. The limits of the deposit are not well defined in the proximity of Pico's flank, covering a minimum area of 32 km^2.
3. A smaller deposit at the base of S. Jorge's southern flank (Fig. 6a, feature "C"), with 4 km of maximum length, measured from, and perpendicularly to, the base of S. Jorge's submarine flank, and covering an area of ca. 12 km^2. Upslope the submarine flank, there is an arcuate-shaped scar (Fig. 6a, red dashed line).
4. Lobate-shaped deposits visible along the base of Pico and S. Jorge's flanks. These deposits are generally composed of small size debris, undistinguishable on the 50 m resolution DEM, but with some larger hummocks.

3.4. Debris volume

The exposed volume of Pico's northern deposit (Fig. 6a, feature "A") was estimated considering solely the space between the actual topographic surface of the deposit and hypothetical basal surfaces (based on submarine flank profiles performed on deposit-free sectors). We built NNE–SSW cross sections of the original grid (perpendicular to the coastline on the zone where the deposit is thickest), spaced approximately 1.2 km, and covering the deposit area and the surrounding deposit-free area (Fig. 7). The origin considered for the horizontal distance of the cross sections is the −100 m contour line, roughly the limit of the Pico's shelf. For the calculation of the exposed volume, we assume that the upward limit of the deposit is at −100 m contour (we assume that it is limited to the extent visible on the bathymetry,

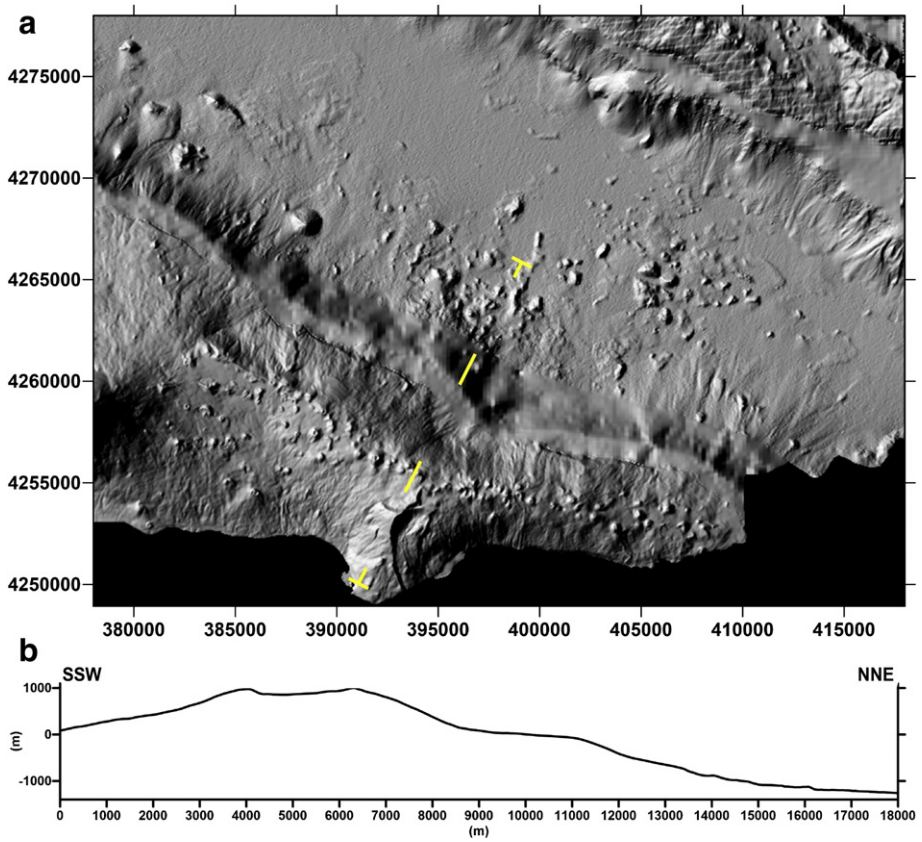

Fig. 5. (a) Shaded relief map of the S. Jorge channel, sub-aerial Pico and S. Jorge islands (lighting from ESE, 50 m resolution DEM). (b) Topographic profile across Pico Island's sub-aerial domain and submarine northern flank, presented as a yellow dashed line in (a).

not continuing landward), and we do not consider the effects of blanketing by more recent volcanic/sedimentary materials.

As the channel deepens and gets narrower towards the ESE (Fig. 4), the volume will be given as an interval: minimum volume estimated with a hypothetical basal profile representative of the WNW limit of the deposit, and maximum volume estimated with a hypothetical basal profile that considers the greater depths of the ESE limit of the deposit. The hypothetical basal profile from the WNW limit of the deposit (Fig. 7b, black dashed line) was determined from the average of closely spaced cross sections (Fig. 7a, full white line cross sections), on a zone relatively undisturbed by the presence of sedimentary deposits or volcanic cones. In order to build the hypothetical basal profile used for the determination of the maximum volume (Fig. 7b, red dashed line), we considered all the cross sections performed perpendicularly to the coast, and determined the maximum depth attained by the bulk of these cross sections for 1 km spaced horizontal distance values.

For the construction of each hypothetical basal surface, we introduced the values determined for the "normal profiles" in the blank area (Fig. 7a, area comprised by the green dashed line) and performed a 200 m resolution spatial interpolation (kriging) (Fig. 8a and b). The standard deviations associated with the interpolation method used have a maximum value of 25 m (Fig. B.1). These spatial interpolations have associated Root Mean Square (RMS) errors within a range of 4.7–5.6 m, and a maximum residue of 26.0 m, for the deposit's blanked area (Table B.1). Though the maximum residue obtained for the complete grid has a value of 145.1 m (Table B.1), this residue was obtained outside the deposit's blanked area, therefore outside the zone considered in the volume calculation (Fig. B.2). We built "deposit thickness" grids by subtracting each of the hypothetical basal surfaces from the real topographic surface (Fig. 8c and d). The maximum thickness of the deposit lies between ca. 238 and 304 m (Table 1). In Fig. 8c and d, it is visible that there are appreciable volumetric anomalies on the surroundings of the limits defined for the deposit, where it would be ideal to have a perfect fit between real and estimated basal surfaces. In order to partially eliminate these anomalies, the volume was calculated only for the deposit's area (Fig. 8c and d, area comprised by the dashed black line). The volume of the deposit visible on the bathymetry is, roughly, between 4 and 10 km^3 (Table 1, positive volume). If we consider that, for the hypothetical maximum depth basal surface, there are still zones on which the basal surface lies above the real topography (Table 1, negative volume), then the exposed volume of the deposit must be closer to 10 km^3 than to 4 km^3.

4. Fieldwork

In order to constrain the age of failure events on Pico's northern flank, we attempted to sample the volcanic sequence affected by the flank failure and the one covering the landslide scar(s). The fieldwork was focused on the zones where it would be more probable to reach the older volcanic sequence affected by the eventual flank failures, i.e., inside deep creeks incising the cascading lavas, and along coastal cliffs close to these features.

On the eastern sector of Pico's N flank, the high coastal cliff has a maximum height of ca. 400 m. It intersects the steep slope zone that defines the eastern embayment (Fig. 3, feature "4"). Along this coastal cliff, the outcropping sequence consists mainly of lava flows that dip to the N on the western sector, whereas lava flows dip to the NE on the eastern sector (Fig. 6a). No major unconformities have been observed on the outcropping sequence. Nevertheless, we sampled a lava flow (Table 2 and Fig. 2, sample Pi10X), as close as possible to the base of the outcropping sequence.

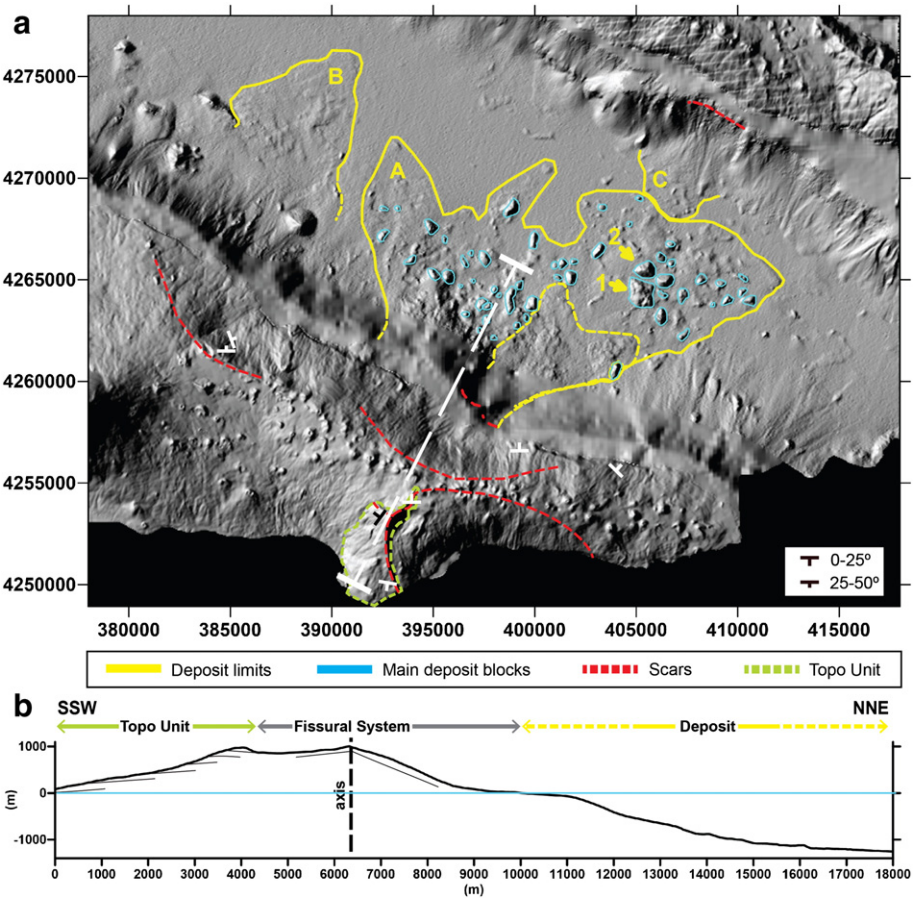

Fig. 6. (a) Shaded relief map of the S. Jorge channel, sub-aerial Pico and S. Jorge islands (lighting from ESE, 50 m resolution DEM), with interpretation of possible scars, blocks and limits of debris deposits. Yellow arrows indicate the biggest individual hummocks observed. Green dashed line indicates the extent of the TU. Dashed white line indicates the cross section presented in b. The lava flow orientations measured on the field are indicated. The non-interpreted version of this shaded relief map is presented as Fig. 5a. (b) Topographic profile across Pico Island and the proximal zone of the main debris deposit interpreted on the bathymetry. Representation of the main geometry of the deposits observed on the field. The non-interpreted version of this topographic profile is presented as Fig. 5b.

On the western sector of Pico's northern flank, we worked upstream along two creeks that incise the zone of steep slope (Fig. 3, feature 5). Here we observed cascading lava flows dipping 35–45° towards the sea (Fig. 6a), intercalated with pyroclastic and clastic sedimentary deposits. Again we could not observe a significant unconformity that could represent a landslide scar. Anyway, we sampled a lava flow at the base of this volcanic sequence (Table 2 and Fig. 2, sample Pi11N). Other samples were collected at the base of coastal cliffs along Pico's northern coast (Table 2 and Fig. 2, samples Pi10R, Pi10P, and Pi10U), in order to constrain the age of the fissural system volcanism.

The easternmost embayment identified on Pico's northern flank is located immediately to the N of the exposed remnants of TU (Figs. 2 and 6a). Additional fieldwork was performed on this sector, in the southern flank of the island (cut by the SSW–NNE cross section presented in Figs. 5 and 6). The observed TU deposits consist mainly of meter thick lava flows with dips in the range 0–25°, and a variation in maximum dip orientation (Fig. 6a). The outcropping TU lavas are limited in the N by a slightly arcuate W–E scarp, ca. 150 m high, whose maximum dip reaches 35–40° towards the N (Fig. 3, feature 6). Near this scarp, the TU lava flows dip 10° towards the NW (Fig. 6a).

5. K–Ar geochronology

The samples were prepared and dated by K–Ar at the IDES laboratory, Université Paris-Sud (Orsay, France). In order to check the unaltered state of the samples, thin sections were carefully observed under the microscope. The samples were crushed and sieved to a homogeneous size fraction (125–250 μm). As phenocrysts may carry inherited excess Ar, by crystallizing previously to the eruption under high pressures at depth, their presence in the analyzed sample may lead to the determination of an excessive age. Therefore, we systematically removed all the phenocrysts (olivine, pyroxene and plagioclase), through magnetic separation and heavy-liquid sorting. At the end of this process, we obtained a groundmass of homogeneous grain size (125–250 μm) and density (classically ranging between 2.95 g/cm^3 and 3.05 g/cm^3 for basaltic samples).

K was measured by flame absorption-spectrophotometry, with 1% uncertainty from systematic analysis of standards (Gillot et al., 1992). Ar was measured by mass spectrometry, according to the Cassignol–Gillot unspiked technique (Cassignol and Gillot, 1982; Gillot and Cornette, 1986; Gillot et al., 2006). The Cassignol–Gillot technique has been shown especially suitable to date low-K and high-Ca basalts and andesites of late Quaternary age with an uncertainty of only a few ka (e.g., Samper et al., 2007; Hildenbrand et al., 2008, 2012a; Germa et al., 2011; Boulesteix et al., 2012, 2013). With this technique, ^{40}Ar and ^{36}Ar are measured simultaneously, avoiding any potential signal drift. Also with this technique, the level of atmospheric contamination is accurately determined by comparison between the isotopic ratios of the sample and an air pipette at strictly similar ^{40}Ar level. This allows the detection of tiny amounts of radiogenic ^{40}Ar, as low as 0.1% (Gillot et al., 2006).

K and Ar were both measured at least twice to ensure the reproducibility of the results. The used decay constants are from Steiger and Jäger (1977). The obtained ages are presented in Fig. 2 and Table 2, where the uncertainties are quoted at the 1σ level. The various lava flows sampled in this study are dated between 70 ± 4 ka and 52 ± 5 ka. The oldest

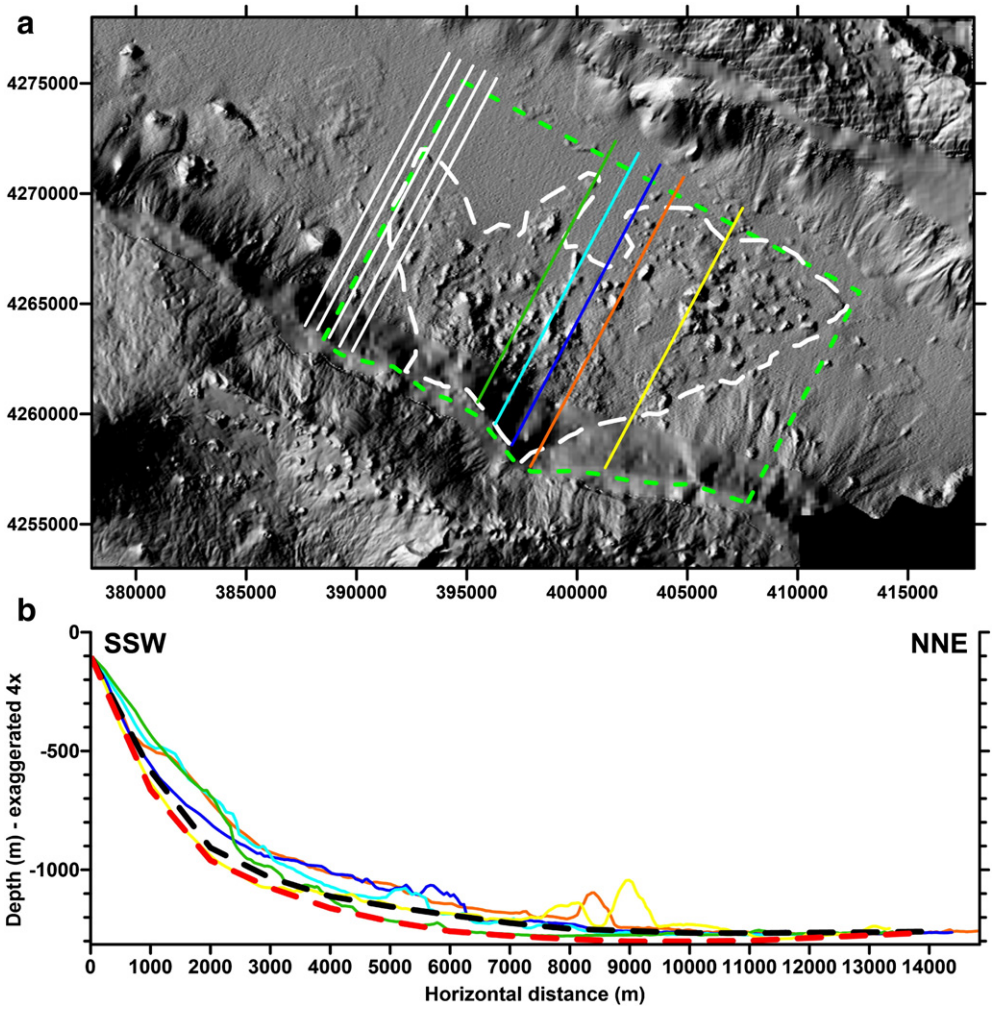

Fig. 7. (a) Full colored lines on the deposit area represent the most relevant NNE–SSW cross sections. Full white lines on the NW represent the cross sections considered for the calculation of the "normal" submarine profile, used in the estimation of minimum volume. Contour of debris deposit is represented by a dashed white line, and the contour of the area blanked for volume calculation purposes is defined by the green dashed line. (b) Plot of the most relevant SSW–NNE cross-sections on the deposit area (full lines) and of the hypothetical basal profiles built for the calculation of minimum volume (red dashed line) and maximum volume (black dashed line).

flows covering the western and eastern scars yield similar values of 70 ± 4 ka and 69 ± 4 ka (samples Pi10X and Pi10 R, respectively).

6. Discussion

6.1. Sub-aerial scarps on Pico's northern flank

Although still very steep on the slope map, the two main curved scarps visible on Pico's sub-aerial N flank are presently smooth, due to blanketing by volcanic products that erupted from the fissural system and Pico stratovolcano. These younger volcanic deposits have therefore been deposited on top of a sharper and steeper scarp. Wide lava deltas have formed at the base of the curved scarps (Figs. 2 and 3), thus smoothing also part of the submarine scarp.

Following Mitchell (2003), who hypothesized a landslide related origin for these conspicuous scarps, we interpret these features as scars resulting from past failure events on Pico's northern flank.

6.2. Main debris deposit

6.2.1. Debris dimensions

Some of the hummocks in the debris deposit A (Fig. 6a) are easily discernible on the shaded relief image due to the strong reflection/shadow contrast of their "soft" surfaces under the imposed lighting. As these hummocks generally have an irregular shape rather than being conical features, we interpret them as blocks rather than small volcanic edifices.

Despite its significant dimensions, the height of the biggest hummock identified (see Section 3.3) is very small when compared to its width/length, and the hummock's surface is extremely irregular and weakly reflects the imposed lighting (Fig. 6a, feature "1", see Section 3.3). We interpret this large hummock as evidence for either a big irregular block or an agglomerate of blocks, covered by smaller debris. The second largest hummock identified (Fig. 6a, feature "2", see Section 3.3) constitutes the biggest individual block observed on the surface of the deposit.

6.2.2. Debris source(s) and number of failure events

Based on the location, shape, and thickness spatial distribution, we interpret this hummocky terrain as a deposit of material resulting from partial collapse of Pico's northern flank. The deposit's shape and thickness spatial distribution at the foot of Pico's submarine flank suggest a source area of relatively small lateral extent (ca. 7 km). This source zone likely corresponds to the sub-aerial scar immediately upstream the deposit (Fig. 6a).

We interpret the homogeneous debris size domain on the SE of the deposit (Fig. 6a, feature A, yellow dashed line) as a deposit resulting from a more recent collapse of Pico's submarine flank. As suggested by the deposit's shape and the longitudinal flow structures visible on its

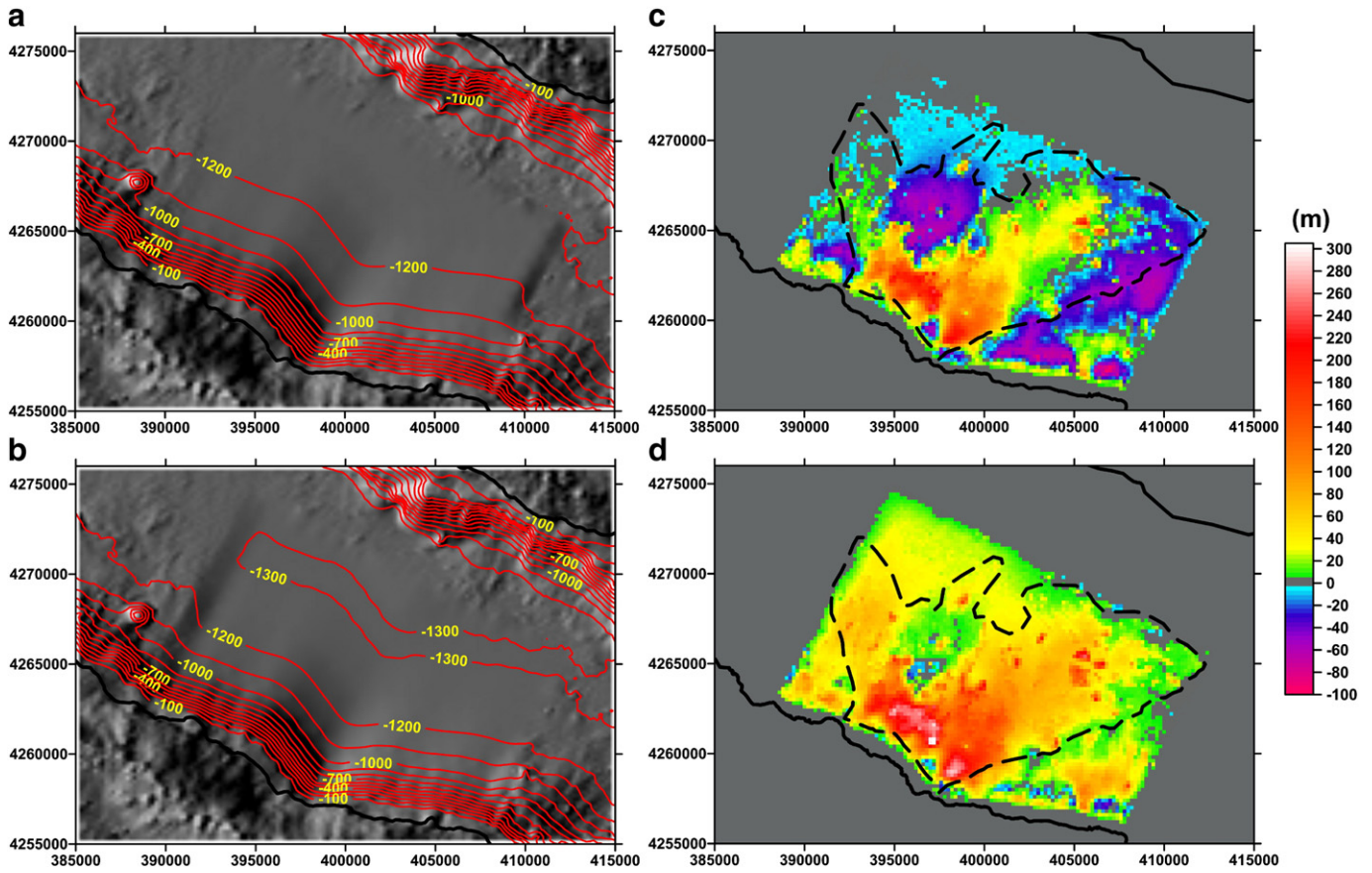

Fig. 8. Estimated basal surfaces for minimum volume (a) and maximum volume (b) calculations (grid lighting from WNW, 0 m contour lines of the surfaces plotted as full black lines). Grids of deposit thickness for the minimum volume (c) and maximum volume (d) (black dashed line limits the area considered for the volume calculations, and the full black lines represent the islands' coastlines). Color scale for the deposit thickness (c and d) is presented on the right.

surface (lineaments mentioned in Section 3.3, visible in Fig. 2 from Mitchell et al., 2008), the interpreted sources of this deposit's material are the two arcuate scarps uphill of the submarine deposit (Fig. 6a). The scars interpreted on the sub-aerial northern flank have been covered by more recent volcanic deposits. The significant protrusion near sea level observable in the area interpreted as source zone of the main deposit (Fig. 6) is interpreted as a consequence of more recent submarine flank reconstruction and lava delta accumulation (Mitchell et al., 2002, 2008; Mitchell, 2003), thus reshaping the scar left by the debris avalanche.

Therefore, it is impossible to assess directly (a) the landward continuity of the deposit (Fig. 9), (b) the exact configuration, at depth, of the scar associated with the failure (Fig. 9, yellow dashed line), and (c) which volcanic sequences were affected by the flank collapse. The possible scenarios for the sequences affected by the studied flank failure were constrained by the local topography (Fig. 6) and fieldwork data, and depend on the premises we assume for: (a) the continuity of the TU volcanic edifice towards the N, where it is masked by deposits of the more recent fissural system; (b) the actual configuration of the scar at depth; and (c) the possible development of a pre-collapse sequence of sub-aerial fissural system deposits.

Three main hypotheses can be put forward regarding the sequences that were affected by the major flank failure identified in this study:

1. The TU volcanic edifice was continuous and higher towards the N, and its northern flank collapsed catastrophically (Fig. 9a);
2. The TU volcanic edifice was shallower towards the N, on top of which a pre-collapse fissural system grew. Then failure occurred in the N, with catastrophic removal of deposits from both TU and pre-collapse fissural edifices (Fig. 9b).
3. The TU volcanic edifice was shallow towards the N, on top of which a thick sequence of pre-collapse fissural system deposits was emplaced. When the N flank failure occurred, only the pre-collapse fissural system was affected (Fig. 9c).

Though hypotheses 2 (Fig. 9b) and 3 (Fig. 9c) cannot be excluded, fieldwork observations on the scar did not allow the identification of a pre-collapse fissural system sequence. Therefore, scenario 1 (Fig. 9a), which considers the failure of TU volcanics only, is here considered as the soundest hypothesis.

Based on this hypothesis, we propose the following evolution for this sector of the volcanic ridge:

1. Growth of the TU volcanic edifice (Fig. 10a and b). The variation of the maximum dip orientation of the volcanic deposits observed in the field (Fig. 10a) suggests that the original summit of this volcanic edifice would be located in the area of the SE Pico active slump depression (Figs. 3 and 10). Such location had already been proposed for the core of the referred volcanic edifice by Nunes et al. (2006), from the interpretation of a major positive Bouger anomaly identified there.
2. Destruction of most of the TU volcanic edifice (Fig. 10c).

Table 1
Values of volume and thickness obtained for the models of minimum and maximum volumes. Positive volume is the volume between the surfaces, being the hypothetical basal surface under the actual topographic surface. Negative volume is the volume between the surfaces, being the hypothetical basal surface above the actual topographic surface.

	Positive volume (km^3)	Negative volume (km^3)	Maximum thickness (m)
Minimum volume	4.278	1.6	238
Maximum volume	10.242	0.015	304

Table 2
Results of the K–Ar dating on fresh-separated groundmass. The ages are indicated in thousands of years (ka). The uncertainties are reported at the 1σ level.

Samples	UTM E	UTM N	K (%)	$^{40}Ar^*$ (%)	$^{40}Ar^*$ (10^{10} at/g)	Age (ka)	Uncertainty (ka)	Mean (ka)
Pi10X	26405050	4255843	0.897	1.7	6.378	68	4	70 ± 4
				1.8	6.715	72	4	
Pi10R	26386933	4262897	1.057	2.3	7.823	71	3	69 ± 4
				1.2	7.116	64	6	
Pi11N	26384950	4261825	0.913	1.9	5.602	59	3	56 ± 4
				1.0	4.949	52	5	
Pi10P	26383509	4265958	0.831	0.5	4.116	47	9	53 ± 5
				1.4	4.788	55	4	
Pi10U	26392413	4260735	0.961	1.0	5.523	55	5	52 ± 5
				0.9	4.951	49	5	

The clear N–S scarp that affects this edifice's eastern sector (Fig. 3, feature "1") shows that part of the mass-wasting has been accommodated along the structure(s) that constitute the currently active large-scale slump structure (mass wasting structure not represented in Figs. 6 and 9, since it is not intersected by the cross section).

It is not possible to observe the continuation of TU edifice towards the N, due to large-scale flank destruction and masking of the remnants by the more recent fissural system deposits (Fig. 10d). The destruction of this edifice's northern flank would have occurred along the sub-aerial scar interpreted for the eastern sector of Pico, and originated the major submarine deposit here reported. The orientation and dip of the exposed north-facing scarp that constitutes the northern limit of TU's outcrops (Fig. 3, feature "6") are not concordant with the local orientation of volcanic deposits (see Section 4). This structure was previously interpreted as a fault scarp (Madeira and Brum da Silveira, 2003), and it might constitute the uppermost expression of a secondary structure located further S of the interpreted main sub-aerial scar (Fig. 10c and d, yellow dashed line with question marks). This interpreted structure could have accommodated non-catastrophic deformation of the TU's volcanic sequence to the S of the main scar.

3. Growth of the fissural system (Fig. 2, FS), masking the sub-aerial scar in TU edifice's northern flank (Fig. 10d). The real configurations of the interpreted scar and of the remnants of the TU volcanic edifice have been extensively masked by more recent volcanism. Therefore it is not possible to establish a detailed comparison between the configuration of the scars identified on Pico's northern flank with landslide scars exposed elsewhere.

Debris deposits resulting from the accumulation of multiple failures have been described in some oceanic islands (e.g. Urgeles et al., 1999; Watts and Masson, 2001; Masson et al., 2006; Hunt et al., 2011). In Pico, with the exception of the homogeneous debris field in the SE

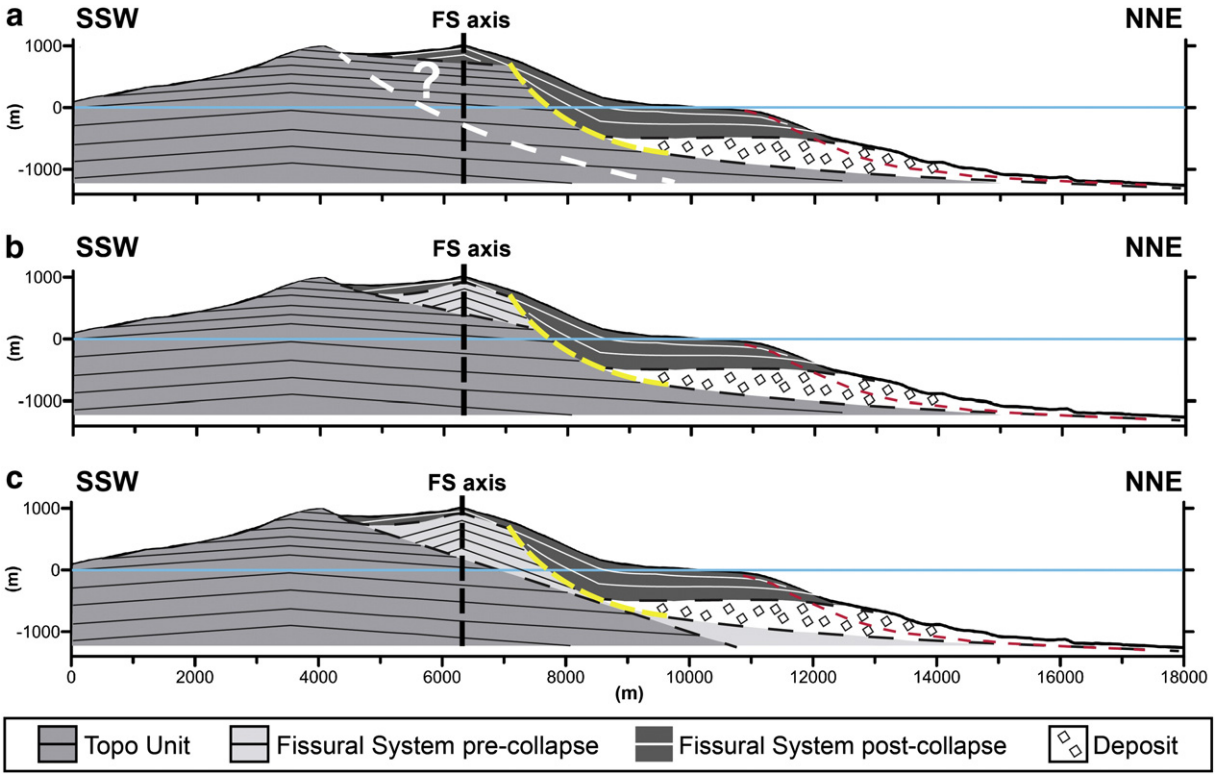

Fig. 9. Geological interpretation of the section marked in Figs. 5 and 6. Yellow dashed line marks the scar suggested as debris source. Red dashed line represents the basal surface considered in the estimation of the maximum volume. Black dashed lines indicate the suggested contacts between volcanic sequences and the deposit. White dashed line indicates a suggested secondary structure that affected TU volcanic sequence. Possible scenarios for the volcanic sequence(s) affected by the flank failure: (a) scar only affects TU deposits; (b) scar affects TU and fissural system deposits; (c) and scar only affects fissural system deposits.

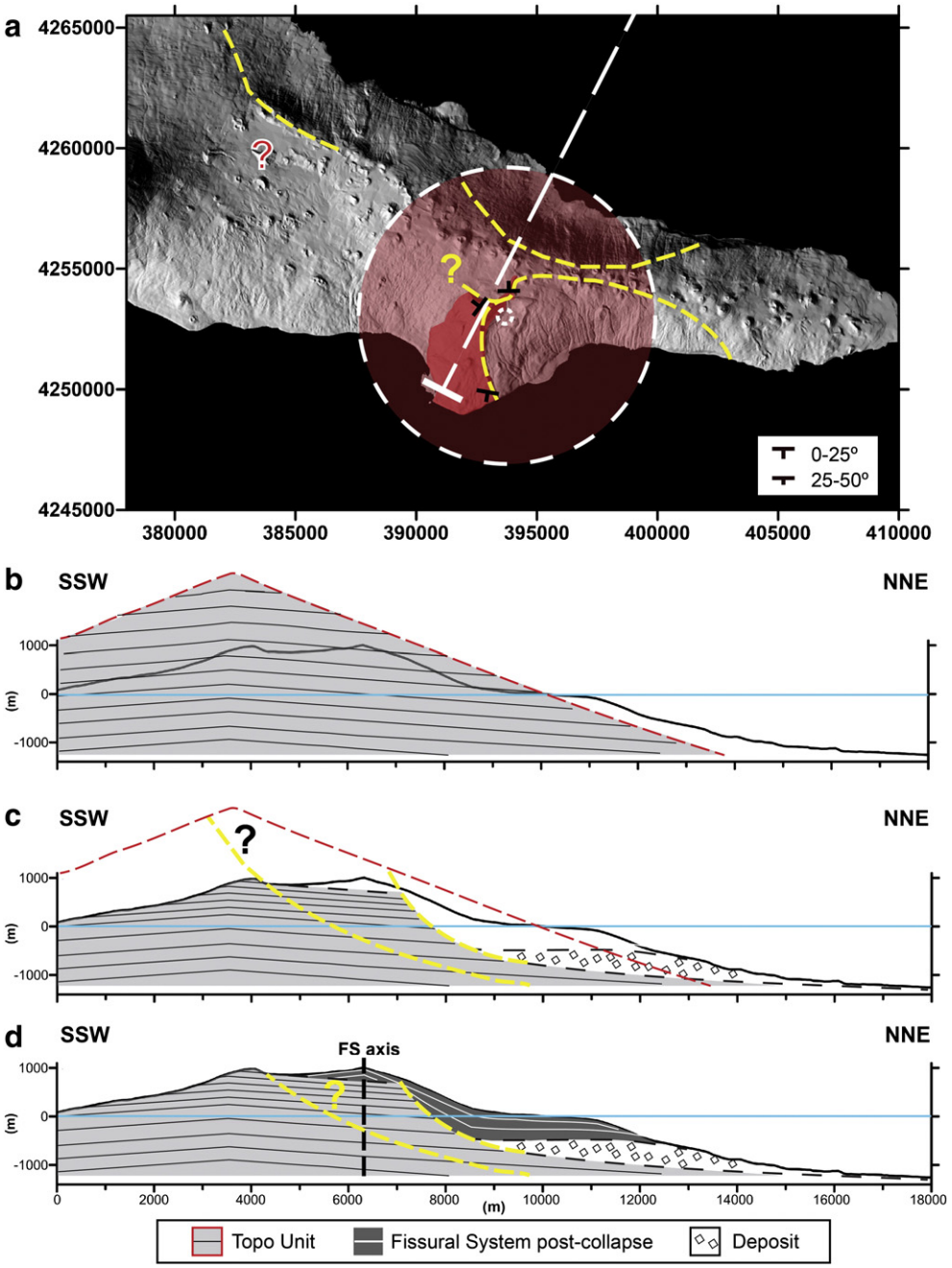

Fig. 10. Presentation of the hypothesis in which the failure that originated the main deposit only affected the TU sequence. (a) Map view of sub-aerial Pico with the representation of the actual extent of sub-aerial TU volcanic edifice (dark red area) and its lava flow orientations, the schematic configuration of the original TU edifice (semi-transparent light red area) and the location of its original crater (small white dashed line circle). SSW–NNE white dashed line represents the cross section interpreted. Yellow dashed lines represent the scarps interpreted in the study area. Schematic representation of the evolution of this volcanic ridge sector, across the SSW–NNE topographic profile: (b) original configuration of TU edifice. (c) TU's northern flank destruction; (d) current stage, with fissural system (FS) deposits concealing the scar of the failure event in study.

sector of the main deposit, and interpreted as resulting from the collapse of the submarine flank, we did not find morphological or chronological evidence supporting the formation of the debris deposit by accumulation of multiple failures. Therefore, we consider that the deposit results from a single failure event, with the exception of a subsequent small failure on the submarine flank.

6.2.3. Debris volume

The lack of data regarding the inner structure of the island (i.e. geophysical data) prevents us from assessing the extent of surface morphology change since the flank failure, due to factors like the partial filling of the topographic embayment by younger volcanic products. However, considering the geometrical constraints imposed by the topography, the geometry/location of the interpreted scar, the geometry of the observed deposit surface offshore, and field data (Fig. 6a), we provide simplified interpreted schemes (Fig. 9) for the inner structure of the island along the cross section presented in Figs. 5 and 6.

The constraints imposed by the location/geometry of the interpreted scar (Fig. 9, yellow dashed line) and by the northern flank topography represented in the cross section suggest the inland continuation of the debris deposit (Fig. 9). Therefore, we consider that even the maximum volume of 10 km^3 here estimated for the exposed part of the deposit (Fig. 9, red dashed line represents the basal surface considered in the

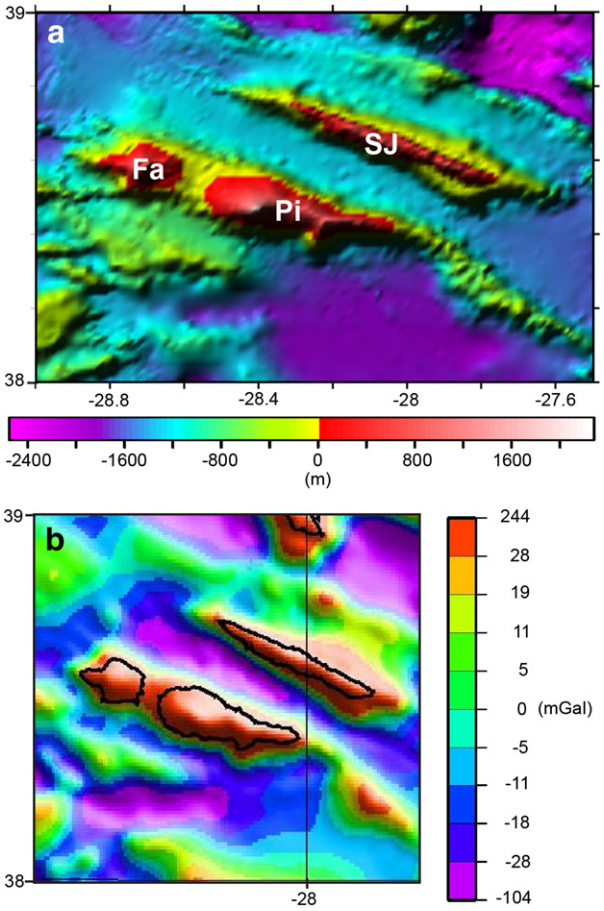

Fig. 11. (a) 1300 resolution DEM (lighting from NW) of the study area. Bathymetric data from Lourenço et al. (1998), available at http://w3.ualg.pt/~jluis/. Fa — Faial Island, Pi — Pico Island, SJ — S. Jorge Island. (b) Free air gravity anomaly map of the same area (extract of Fig. 3 from Catalão and Bos, 2008).

estimation of the maximum volume observable) will constitute an underestimation of the actual volume of the debris deposit.

Catalão and Bos (2008) present a free air gravity anomaly map of the Azores (Fig. 11b, extract of Fig. 3 in Catalão and Bos, 2008), produced from land gravity data, ship-borne gravity data, and a background grid of satellite altimeter-derived gravity data (model KMS02, from Andersen et al., 1999). In order to avoid possible anomalies of the satellite data near the steep coastlines of the islands, these data were not considered for offshore areas at less than 20 km from the coastlines (the coastlines were masked with a 20 km buffer on the offshore domain) (Catalão and Bos, 2008).

This map of the free air gravity anomaly (Fig. 11b) displays a strong negative anomaly in the S. Jorge Channel. However, it is clear from the bathymetry (Fig. 11a) that this area does not correspond to a strong topographic low. Note that the deep basins (magenta in Fig. 11a) correspond to strong negative gravity anomalies (magenta in Fig. 11b). Therefore, we interpret the contrasting association of high topography (green in Fig. 11a) and strong negative gravity anomaly as the result of accumulation of a rock with density much lower than basalt, most likely corresponding to thick accumulation of marine sediments (low density deposits). The thick accumulation of sediments may have blanketed the debris deposits, thus concealing their actual dimensions.

Therefore, considering the probable inland continuation of the deposit (Fig. 9) and the masking of the actual deposit by more recent blanketing by volcanic/sedimentary products, we conclude that the actual volume probably exceeds the estimated 10 km^3.

6.2.4. Flow mobility and constraints

The deposit's shape and the debris distribution in the deposit suggest that part of the debris flowed towards NNW and NNE, but the most significant part of the landslide material (including the biggest blocks) flowed towards greater depths towards the E. It was thus clearly conditioned by the submarine topography.

The mobility of a landslide can be expressed as a function of the ratio H/L (H — height between the topmost source zone of the material and the deposit; L — maximum runout length), which represents the apparent coefficient of friction of the avalanche (e.g. Lipman et al., 1988; Hampton et al., 1996). This ratio decreases (mobility increases) for material volumes larger than 0.001 km^3 (Scheidegger, 1973, in Hampton et al., 1996). More recently, Legros (2002) argued that L is mainly controlled by the volume (V) of the failed mass, instead of being controlled by H.

The estimated maximum volume of Pico's debris deposit is ca. 10 km^3, L is ca. 22 km (measured along a longitudinal profile), and H is ca. 2 km. The estimated volume is below, and the ratio H/L is above the values given for volcanic submarine landslides in Legros (2002). The graphs in Fig. 12 show correlations between H, L, V and H/L data from several oceanic islands' landslide deposits (data presented in Table 3). From the graph in Fig. 12c it is clear that the mobility of Pico's debris deposit, the smallest deposit plotted, broadly fits the trend of decreasing H/L for decreasing volume values. Though the control imposed by the buttressing S. Jorge flank is clear in the morphological analysis of the deposit, its effect on the landslide mobility (i.e., effect on the runout distance reached by the deposit) is not clear in the graphical analysis.

6.2.5. Configuration, block dimensions and spatial distribution

The general shape of the studied deposit is very similar to that of Güimar's debris deposit, resulting from the destabilization of a growing volcanic ridge on the SE flank of Tenerife Island (Canary Islands) (Krastel and Schmincke, 2002), and to that of Monte Amarelo's debris deposit, resulting from the destabilization of Fogo Island (Cape Verde) (Le Bas et al., 2007; Masson et al., 2008). Similarly to Pico, the landslide products in Tenerife and Fogo were mostly constrained by submarine channels: the Güimar landslide products were confined to the channel between Tenerife and Gran Canaria islands, and the Monte Amarelo's landslide products have been confined to the channel between Fogo and Santiago Islands. As recognized by Mitchell et al. (2008) for the sector of Pico's deposit most proximal to its source, the spatial distribution of debris is similar to one of the deposits on west La Palma, which resulted from the accumulation of debris from more than one landslide event (Playa de la Veta Debris Avalanche Complex, and Cumbre Nueva Debris Avalanche, Urgeles et al., 1999).

There are no clearly observed erosional chutes between the source zone and Pico's debris deposit, unlike many cases identified offshore some of the Canary and Hawaiian Islands (Mitchell et al., 2002). We consider that the absence of a well defined chute in Pico's deposit is due to the combination of a relatively small runout (imposed, at least in part, by the nearby topographic obstacle of the S. Jorge ridge), and the extensive masking of the source and proximal sector of the deposit by more recent volcanic products.

Though the maximum runout and volume of Pico's deposit are at least one order of magnitude lower than giant landslides recognized in other oceanic volcanoes (Canary, Hawaii), the largest block dimensions are similar to the ones observed in the Canaries (e.g.,; Masson, 1996; Krastel et al., 2001; Watts and Masson, 2001), but much smaller than the largest blocks exposed offshore the Hawaiian islands (e.g., Moore et al., 1995).

While in Güimar's deposit the largest blocks are observed in the most proximal sector of the deposit, the largest blocks visible in Pico's northern deposit are located on the distal sector of the deposit. A similar spatial arrangement of the blocks has been observed in other deposits found in Hawaii (e.g., South Kona deposit in the SW of Hawaii island —

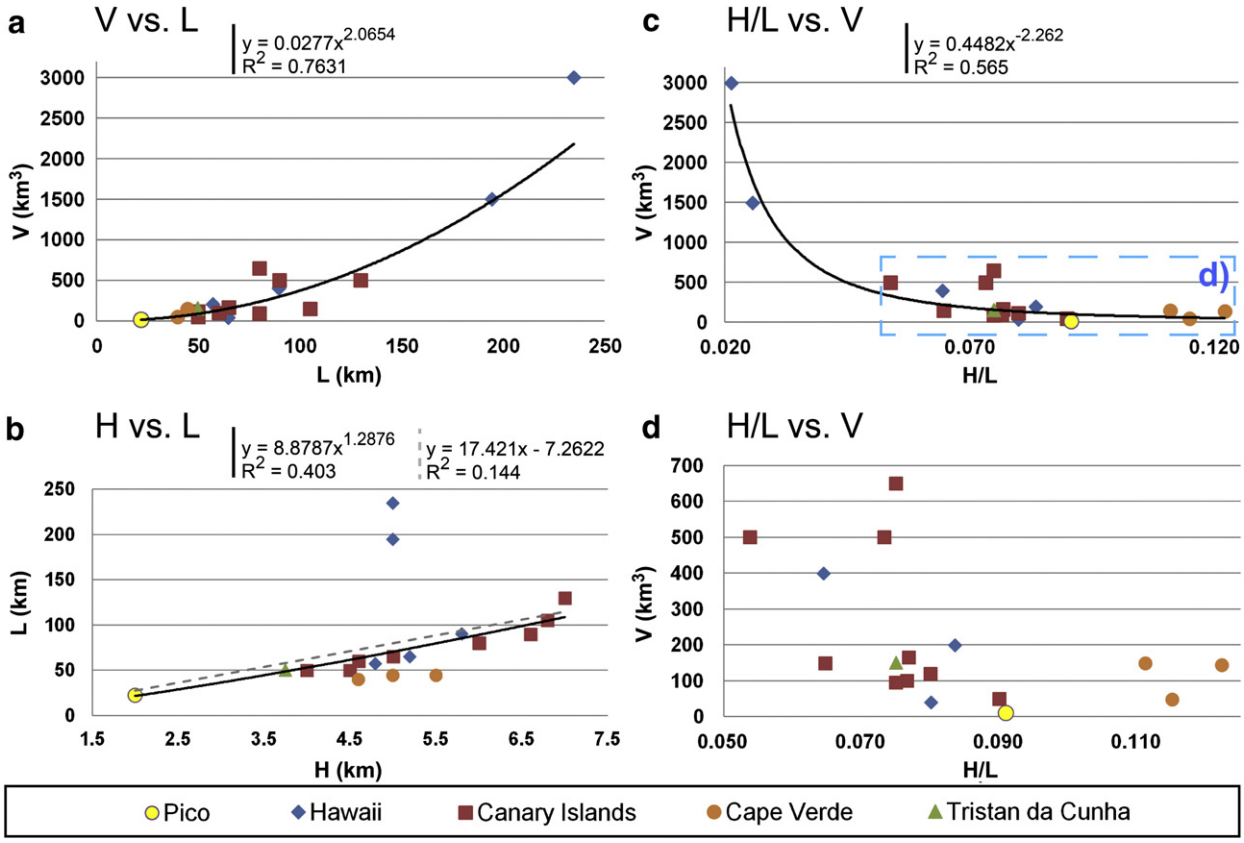

Fig. 12. Plots of correlation between maximum runout length (*L*) (km), height (*H*) (km), ratio *H*/*L*, and volume (*V*) (km^3) for volcanic landslides in oceanic islands. Values plotted (Hawaii Islands, Canary Islands, Tristan da Cunha, Cape Verde and Pico) and respective references are indicated in Table 3. Graphical representation, equation and coefficient of determination (R^2) of power law trend lines (full black lines) and linear trend line (gray dashed line).

Table 3
Data from landslides of Hawaii Islands, Canary Islands, Tristan da Cunha Island, Cape Verde Islands, and Pico Island, plotted in Fig. 12.

Island	Landslide	Volume (km^3)	*L* (km)	*H* (km)	*H*/*L*	References
Azores Islands						
Pico		>10	22	2	0.091	This study
Hawaii Islands						
Hawaii	Alika–1	400	80–100[a]	5.8	0.064	Lipman et al. (1988)
	Alika–2	200	55–60[a]	4.8	0.083	Lipman et al. (1988)
	Kae Lae slide	40	65	5.2	0.080	Legros (2002)
Molokai	Wailau slide	1500	<195	5	0.026	Moore et al. (1989), Moore and Clague (2002), Satake et al. (2002)
Oahu	Nuuanu	3000	235	5	0.021	Moore et al. (1989), Moore and Clague (2002), Satake et al. (2002)
Tristan da Cunha Islands						
Tristan da Cunha		150	50	3.75	0.075	Hampton et al. (1996)
Canary Islands						
El Hierro	El Golfo	150–180[a]	65	5	0.077	Masson et al. (2002)
	Las Playas II	<50	50	4.5	0.090	Masson et al. (2002)
	El Julan	130 (?)	60	4.6	0.077	Masson et al. (2002)
La Palma	Cumbre Nueva	95	80	6	0.075	Masson et al. (2002)
	Playa de la Veta	650 (?)	80	6	0.075	Masson et al. (2002)
Tenerife	Icod	150 (?)	105	6.8	0.065	Masson et al. (2002)
	Roques de Garcia	500 (?)	130	7	0.054	Masson et al. (2002)
	Orotava	500 (?)	90	6.6	0.073	Masson et al. (2002)
	Güimar	120	> 50	4	0.080	Masson et al. (2002)
Cape Verde						
Fogo	Monte Amarelo	130–160[a]	45	5.5	0.122	Day et al. (1999), Masson et al. (2008)
Santo Antão	Tope de Coroa 2	50	40	4.6	0.115	Holm et al. (2006), Masson et al. (2008)
	Tope de Coroa 1	150	45	5	0.111	Holm et al. (2006), Masson et al. (2008)

[a] For dimensions given as intervals, the value plotted was the average of the interval range.

Moore et al., 1995) and Canary Islands (e.g., Icod deposit to the N of Tenerife, where relatively large blocks are concentrated along the margins of the deposit — Watts and Masson, 2001), which have been interpreted as evidence of the high velocity of the avalanches.

The comparatively smaller size of debris in the Canaries relative to Hawaii has been interpreted as being caused by several possible factors and processes: (1) block interaction and disintegration caused by confined flow along narrow chutes (Mitchell et al., 2002); (2) relatively more important component of failed sub-aerial material in Canary Islands, which would promote a more effective disintegration, due to a confining pressure lower in the sub-aerial domain than in the submarine domain (Mitchell et al., 2002); and (3) another factor that might influence the disintegration process is the higher proportion of pyroclastic material in the Canary, which will be more prone to disintegration than sequences constituted mainly by basaltic intrusive/extrusive rocks with a minor pyroclastic component (Mitchell et al., 2002, after Masson et al., 2002).

The debris transport in Pico's deposit was comparatively shorter and involved a smaller volume of material than the ones in Hawaii and the Canary (Fig. 12a). Moreover, the remnants of the edifice interpreted as the main source of northern Pico event(s) comprise a sequence mostly made of shallow dipping, meter thick lava flows, with no significant pyroclastic deposits. Therefore, the disintegration process in the Pico's event should be less effective than for the events in the Canary Islands.

6.3. Minor debris deposits

The shape of the "B" debris deposit (Fig. 6a) shows that it resulted from the accumulation of material transported from Pico's flank. However, it is not possible to define a source for this material as the limits of the deposit are undefined near Pico's submarine flank: it could result simply from the gradual accumulation of material from Pico's submarine flank; or it could be the relict of the deposit resulting from the collapse along the interpreted westernmost sub-aerial scar, now almost completely masked by the younger volcanic deposits.

The "C" debris deposit (Fig. 6a) is interpreted here as having resulted from a collapse of the uphill submarine flank of S. Jorge, where a scar is still visible (Fig. 6a, red dashed line).

6.4. Age of Pico's northern flank failure(s)

Previous K–Ar ages published on Pico (Féraud et al., 1980; Demande et al., 1982; Fig. 2) were acquired on a limited number of samples, and therefore do not constrain accurately the evolution of the island. Some of those previous ages also must be considered with caution, as they have been acquired on whole-rock samples, which can significantly bias the results, as discussed in Hildenbrand et al. (2012a).

On Pico's northern flank, we only observed outcrops of the volcanic deposits that cover the interpreted scar depressions (see Section 4), therefore the new K–Ar ages here obtained on fresh groundmass only provide a minimum age for the flank failure(s). The maximum age of 70 ± 4 ka and 69 ± 4 ka here obtained on the lava flows Pi10X and Pi10 R filling the sub-aerial scars (Fig. 2 and Table 2), provides a minimum age of ca. 70 ka for the occurrence of large-scale collapse(s) in Pico's northern flank.

Based on our data, we cannot establish if the two sub-aerial scarps here identified on Pico's northern flank were produced by two synchronous flank collapses. For the scar interpreted on the western sector of the fissural system (Fig. 3, feature "2"), there is not a corresponding major deposit offshore. As mentioned in Section 6.2, the flank failure deposits might appear masked by more recent volcanic/sedimentary products. As the deposit corresponding to the eastern sub-aerial scar is still clearly visible, this could suggest that the western scar is older than the eastern.

6.5. Possible causes and consequences

Given the geologic setting of the studied volcanic edifice, a steep volcanic ridge located on a tectonically active region, catastrophic failure of Pico northern flank may have been influenced/triggered from a variety of possible processes:

1. Progressive destabilization due to flank overload and oversteepening of TU edifice and/or along the tectonically controlled WNW–ESE volcanic ridge;
2. Triggering by NNE–SSW magma push (associated to the growth of Pico–Faial WNW–ESE volcanic ridge);
3. Fluid overpressure directly or indirectly associated with volcanic activity;
4. Local focusing of destabilization promoted by the physical discontinuity between the TU edifice surface and the fissural system deposits (Fig. 10).

Mitchell (2003) suggests a height threshold of ca. 2.5 km, above which large-scale landslides become common. Previously, Mitchell (2001) suggested that the transition between stable and unstable conditions for submarine volcanic edifices would occur gradually for an interval of edifice heights between 2 and 4 km. The height between Pico's highest point and the sea bottom is above this threshold, i.e. ca. 3.6 km. However, this maximum is attained for Pico stratovolcano, on the westernmost sector of the island, i.e. far from the studied failure. The current height between the topmost level of the source zone and the studied debris deposit is ca. 2 km. When discussing the edifice height at the time of the occurrence of a large-scale landslide, we should take into account that the current configuration of the island does not necessarily correspond to the configuration of the island at the time the landslide occurred. From the absolute ages here presented for Pico, it is not clear that the Pico stratovolcano was already developing by the time the studied flank collapse occurred. However, there was the TU volcano, whose original size and maximum altitude are not known. Therefore, the current height of ca. 2 km between the topmost sector of the source zone and the surrounding submarine floor probably constitutes an underestimation of the height at the time the flank collapse occurred. Considering that the height of the affected volcanic edifice relative to the surrounding sea floor was greater than ca. 2 km, the studied event supports the trend presented in Mitchell (2001).

One of the most important consequences of catastrophic flank collapses on volcanic ocean islands lies in their ability to trigger large tsunamis. Considering that S. Jorge lies to the north of Pico, only ca. 20 km apart, the sudden collapse of a sector several km^3 in dimension would have generated a large tsunami that most likely strongly impacted the southern coast of S. Jorge. Therefore, further investigations should focus on the southern coast of S. Jorge.

6.6. Flank failure in northern and southern Pico

The scar in northern Pico is mirrored in the S flank by a steep slope embayment that includes the currently active slump (Fig. 3, feature "1"). On the offshore area adjacent to this embayment on the southern flank there is a significant deposit whose debris were identified on side scan sonar data (Mitchell, 2003), and which constitutes a topographic bulge on the low resolution bathymetry (see Fig. C.1, in Appendix C). Therefore, both Pico's flanks have been affected by large-scale flank failure, highlighting the strong susceptibility of steep ridge-shaped edifices to flank failure.

7. Conclusions

From the new geomorphologic, stratigraphic, structural and geochronologic data acquired in the present study, we conclude that the evolution of the Pico Island volcanic ridge was marked by the

occurrence of flank failures in both N and S flanks. The landslide debris resulting from the collapse of Pico's N flank have accumulated on the ocean floor of the S. Jorge Channel, and their likely sources are two major scars standing out on Pico's slope map.

Here we conclude that, more than 70 ka ago, after the growth of the TU volcanic edifice, Pico's northern flank collapsed catastrophically, forming two steep and arcuate sub-aerial scars. The material mobilized from the eastern source zone likely exceeds 10 km^3, and consists of a mixture of meter to hectometer blocks. These flowed towards greater depths in the E, along the channel between Pico–Faial and S. Jorge volcanic ridges. The tsunami resulting from the km^3 collapse most probably rapidly traveled the ca. 20 km wide channel and violently impacted S. Jorge's southern flank. Since ca. 70 ka and until historic times, more recent deposits, volcanic products related to the growth of the WNW–ESE fissural system and Pico stratovolcano have been progressively filling the sub-aerial scars. These post-collapse volcanic products, and marine sediments as well, have been covering the island's submarine flanks, masking partially or completely the evidence of failure events.

The evolution of the Pico's sector in the Pico–Faial volcanic ridge was also marked by large-scale flank failure on the southern flank, generating a sub-aerial scar (symmetrical to the easternmost scar in the N flank) and a debris deposit observed on the offshore. Further investigations are being conducted, in order to constrain the evolution of this volcanic ridge.

Supplementary data to this article can be found online at http://dx.doi.org/10.1016/j.jvolgeores.2014.01.002.

Acknowledgments

This is a contribution to Project MEGAHazards, funded by FCT (PTDC/CTE-GIX/108149/2008), Portugal. The first author has a PhD scholarship funded by FCT (SFRH/BD/68983/2010). We thank EMEPC (http://www.emepc.pt/), and Nuno Lourenço in particular, for making the bathymetric data available, without which this study would not have been possible. The final version of this paper benefited from the constructive and thorough comments by N. Mitchell.

References

Afonso, A., Gomes, F., Fernandes, M., 2002. IGeoE: Cartografia de qualidade - a base de um SIG. Trib. das Autarquias 108, 13–14 (Jun. 2002).

Andersen, O.B., Knudsen, P., Kenyon, S., Trimmer, R., 1999. Recent improvement in the KMS global marine gravity field. Boll. Geofis. Teor. Appl. 40 (3–4), 369–377.

Borges, J.F., Bezzeghoud, M., Buforn, E., Pro, C., Fitas, A., 2007. The 1980, 1997 and 1998 Azores earthquakes and some seismo-tectonic implications. Tectonophysics 435 (1–4), 37–54. http://dx.doi.org/10.1016/j.tecto.2007.01.008.

Boulesteix, T., Hildenbrand, A., Gillot, P.Y., Soler, V., 2012. Eruptive response of oceanic islands to giant landslides: new insights from the geomorphologic evolution of the Teide–Pico Viejo volcanic complex (Tenerife, Canary). Geomorphology 138 (1), 61–73. http://dx.doi.org/10.1016/j.geomorph.2011.08.025.

Boulesteix, T., Hildenbrand, A., Soler, V., Quidelleur, X., Gillot, P.Y., 2013. Coeval giant landslides in the Canary Islands: implications for global, regional and local triggers of giant flank collapses on oceanic volcanoes. J. Volcanol. Geotherm. Res. 257, 90–98. http://dx.doi.org/10.1016/j.jvolgeores.2013.03.008.

Burrough, P.A., McDonnell, R.A., 1998. Principles of Geographical Information Systems. Oxford University Press, New York (333 pp.).

Carracedo, J.C., Day, S.J., Guillou, H., Torrado, F.J.P., 1999. Giant Quaternary landslides in the evolution of La Palma and El Hierro, Canary Islands. J. Volcanol. Geotherm. Res. 94 (1–4), 169–190. http://dx.doi.org/10.1016/S0377-0273(99)00102-X.

Cassignol, C., Gillot, P.Y., 1982. Range and effectiveness of unspiked potassium–argon dating: experimental groundwork and applications. In: Odin, G.S. (Ed.) Numerical Dating in Stratigraphy. John Wiley & Sons Ltd, Chichester, England, pp. 159–179.

Catalão, J., Bos, M.S., 2008. Sensitivity analysis of the gravity geoid estimation: a case study on the Azores plateau. Phys. Earth Planet. Inter. 168 (1–2), 113–124. http://dx.doi.org/10.1016/j.pepi.2008.05.010.

Day, S.J., Heleno da Silva, S.I.N., Fonseca, J.F.B.D., 1999. A past giant lateral collapse and present-day flank instability of Fogo, Cape Verde Islands. J. Volcanol. Geotherm. Res. 94 (1–4), 191–218. http://dx.doi.org/10.1016/S0377-0273(99)00103-1.

Demande, J., Fabriol, R., Gérard, A., Iundt, F., 1982. Prospection géothermique des Iles de Faial et Pico (Açores). Report 82SGN003GTH, Bureau de Recherches Géologiques et Minières, Orléans, France.

Deplus, C., Le Friant, A., Boudon, G., Komorowski, J.C., Villemant, B., Harford, C., Ségoufin, J., Cheminée, J.L., 2001. Submarine evidence for large-scale debris avalanches in the Lesser Antilles Arc. Earth Planet. Sci. Lett. 192 (2), 145–157. http://dx.doi.org/10.1016/S0012-821X(01)00444-7.

Duffield, W.A., Stieltjes, L., Varet, J., 1982. Huge landslide blocks in the growth of Piton de la Fournaise, La Réunion and Kilauea volcano, Hawaii. J. Volcanol. Geotherm. Res. 12 (1–2), 147–160. http://dx.doi.org/10.1016/0377-0273(82)90009-9.

Féraud, G., Kaneoka, I., Allègre, C.J., 1980. K/Ar ages and stress pattern in the Azores: geodynamic implications. Earth Planet. Sci. Lett. 46 (2), 275–286. http://dx.doi.org/10.1016/0012-821X(80)90013-8.

Fernandes, R.M.S., Bastos, L., Miranda, J.M., Lourenço, N., Ambrosius, B.A.C., Noomen, R., Simons, W., 2006. Defining the plate boundaries in the Azores region. J. Volcanol. Geotherm. Res. 156 (1–2), 1–9. http://dx.doi.org/10.1016/j.jvolgeores.2006.03.019.

Forjaz, V.H., 1966. Carta geológica do sistema vulcânico Faial-Pico-S. Jorge. Escala 1:200 000. In: Machado, F., Forjaz, V.H. (Eds.),A actividade vulcânica na ilha do Faial (1957-67), 1968. Comissão de Turismo da Horta, 89 pp.

Germa, A., Quidelleur, X., Lahitte, P., Labanieh, S., Chauvel, C., 2011. The K–Ar Cassignol–Gillot technique applied to western Martinique lavas: a record of Lesser Antilles arc activity from 2 Ma to Mount Pelée volcanism. Quat. Geochronol. 6 (3–4), 341–355. http://dx.doi.org/10.1016/j.quageo.2011.02.001.

Gillot, P.Y., Cornette, Y., 1986. The Cassignol technique for potassium–argon dating, precision and accuracy: examples from the Late Pleistocene to Recent volcanics from southern Italy. Chem. Geol. Isot. Geosci. Sect. 59, 205–222. http://dx.doi.org/10.1016/0168-9622(86)90072-2.

Gillot, P.Y., Cornette, Y., Max, N., Floris, B., 1992. Two reference materials, trachytes MDO-G and ISH-G, for Argon dating (K–Ar and $^{40}Ar/^{39}Ar$) of Pleistocene and Holocene rocks. Geostand. Newslett. 16 (1), 55–60. http://dx.doi.org/10.1111/j.1751-908X.1992.tb00487.x.

Gillot, P.Y., Lefèvre, J.C., Nativel, P.E., 1994. Model for the structural evolution of the volcanoes of Réunion Island. Earth Planet. Sci. Lett. 122 (3–4), 291–302. http://dx.doi.org/10.1016/0012-821X(94)90003-5.

Gillot, P.Y., Hildenbrand, A., Lefèvre, J.C., Albore-Livadie, C., 2006. The K/Ar dating method: principle, analytical techniques and application to Holocene volcanic eruptions in Southern Italy. Acta Vulcanol. 18, 55–66.

Golden Software, Inc., 2002. Surfer 8: contouring and 3D surface mapping for scientists and engineers—user guide. In: Golden Software, Incorporated (Ed.). 640 pp.

Hampton, M.A., Lee, H.J., Locat, J., 1996. Submarine landslides. Rev. Geophys. 34 (1), 33–59. http://dx.doi.org/10.1029/95RG03287.

Hildenbrand, A., Gillot, P.Y., Bonneville, A., 2006. Offshore evidence for a huge landslide of the northern flank of Tahiti–Nui (French Polynesia). Geochemistry Geophysics Geosystems 7 (3), Q03006. http://dx.doi.org/10.1029/2005GC001003.

Hildenbrand, A., Madureira, P., Ornelas Marques, F., Cruz, I., Henry, B., Silva, P., 2008. Multi-stage evolution of a sub-aerial volcanic ridge over the last 1.3 Myr: S. Jorge Island, Azores Triple Junction. Earth Planet. Sci. Lett. 273 (3–4), 289–298. http://dx.doi.org/10.1016/j.epsl.2008.06.041.

Hildenbrand, A., Marques, F.O., Costa, A.C.G., Sibrant, A.L.R., Silva, P.M.F., Henry, B., Miranda, J.M., Madureira, P., 2012a. Reconstructing the architectural evolution of volcanic islands from combined K/Ar, morphologic, tectonic, and magnetic data: the Faial Island example (Azores). J. Volcanol. Geotherm. Res. 241–242, 39–48. http://dx.doi.org/10.1016/j.jvolgeores.2012.06.019.

Hildenbrand, A., Marques, F.O., Catalão, J., Catita, C.M.S., Costa, A.C.G., 2012b. Large-scale active slump of the southeastern flank of Pico Island, Azores. Geology 40 (10), 939–942. http://dx.doi.org/10.1130/G33303.1.

Hildenbrand, A., Marques, F.O., Costa, A.C.G., Sibrant, A.L.R., Silva, P.F., Henry, B., Miranda, J.M., Madureira, P., 2013a. Reply to the comment by Quartau and Mitchell on "Reconstructing the architectural evolution of volcanic islands from combined K/Ar, morphologic, tectonic, and magnetic data: the Faial Island example (Azores)", J. Volcanol. Geotherm. Res. 241–242, 39–48, by Hildenbrand et al. (2012). J. Volcanol. Geotherm. Res. 255, 127–130. http://dx.doi.org/10.1016/j.jvolgeores.2013.01.015.

Hildenbrand, A., Marques, F.O., Catalão, J., Catita, C.M.S., Costa, A.C.G., 2013b. Large-scale active slump of the southeastern flank of Pico Island, Azores: reply. Geology 41 (12), e302. http://dx.doi.org/10.1130/G34879Y.1.

Holm, P.M., Wilson, J.R., Christensen, B.P., Hansen, L., Hansen, S.L., Hein, K.M., Mortensen, A.K., Pedersen, R., Plesner, S., Runge, M.K., 2006. Sampling the Cape Verde mantle plume: evolution of melt compositions on Santo Antão, Cape Verde Islands. J. Petrol. 47 (1), 145–189. http://dx.doi.org/10.1093/petrology/egi071.

Hunt, J.E., Wynn, R.B., Masson, D.G., Talling, P.J., Teagle, D.A.H., 2011. Sedimentological and geochemical evidence for multistage failure of volcanic island landslides: a case study from Icod landslide on north Tenerife, Canary Islands. Geochem. Geophys. Geosyst. 12 (12), Q12007. http://dx.doi.org/10.1029/2011GC003740.

Kongsberg, S., 2007. EM 120 Multibeam Echo Sounder, Product Description. Kongsberg Maritime AS, Norway, Bremerhaven, Pangaea 44 p. (available at http://epic.awi.de/26725/1/Kon2007a.pdf).

Krastel, S., Schmincke, H.U., 2002. The channel between Gran Canaria and Tenerife: constructive processes and destructive events during the evolution of volcanic islands. International Journal of Earth Sciences 91 (4), 629–641. http://dx.doi.org/10.1007/s00531-002-0285-8.

Krastel, S., Schmincke, H.U., Jacobs, C.L., Rihm, R., Le Bas, T.P., Alibés, B., 2001. Submarine landslides around the Canary Islands. J. Geophys. Res. 106 (B3), 3977–3997. http://dx.doi.org/10.1029/2000JB900413.

Le Bas, T.P., Masson, D.G., Holtom, R.T., Grevemeyer, I., 2007. Slope failures on the flanks of the southern Cape Verde Islands. In: Lykousis, V., Sakellariou, D., Locat, J. (Eds.), Submarine Mass Movements and Their Consequences. Springer, Dordrecht, Netherlands, pp. 337–345.

Le Friant, A., Boudon, G., Deplus, C., Villemant, B., 2003. Large-scale flank collapse events during the activity of Montagne Pelée, Martinique, Lesser Antilles. J. Geophys. Res. Solid Earth 108 (B1), 2055. http://dx.doi.org/10.1029/2001JB001624.

Legros, F., 2002. The mobility of long-runout landslides. Eng. Geol. 63 (3–4), 301–331. http://dx.doi.org/10.1016/S0013-7952(01)00090-4.
Lipman, P.W., Normark, W.R., Moore, J.G., Wilson, J.B., Gutmacher, C.E., 1988. The giant submarine Alika debris slide, Mauna Loa, Hawaii. J. Geophys. Res. Solid Earth 93 (B5), 4279–4299. http://dx.doi.org/10.1029/JB093iB05p04279.
Lourenço, N., Miranda, J.M., Luis, J.F., Ribeiro, A., Mendes Victor, L.A., Madeira, J., Needham, H.D., 1998. Morpho-tectonic analysis of the Azores Volcanic Plateau from a new bathymetric compilation of the area. Mar. Geophys. Res. 20 (3), 141–156. http://dx.doi.org/10.1023/A%3A1004505401547.
Madeira, J., 1998. Estudos de neotectónica nas ilhas do Faial, Pico e S. Jorge: Uma contribuição para o conhecimento geodinâmico da junção tripla dos Açores. PhD thesis Faculdade de Ciências, Univ, Lisboa, Portugal (481 pp.).
Madeira, J., Brum da Silveira, A., 2003. Active tectonics and first paleoseismological results in Faial, Pico and S. Jorge islands (Azores, Portugal). Ann. Geophys. 46 (5), 733–761. http://dx.doi.org/10.4401/ag-3453.
Marques, F.O., Catalão, J.C., DeMets, C., Costa, A.C.G., Hildenbrand, A., 2013. GPS and tectonic evidence for a diffuse plate boundary at the Azores Triple Junction. Earth and Planetary Science Letters 381, 177–187. http://dx.doi.org/10.1016/j.epsl.2013.08.051.
Masson, D.G., 1996. Catastrophic collapse of the volcanic island of Hierro 15 ka ago and the history of landslides in the Canary Islands. Geology 24 (3), 231–234. http://dx.doi.org/10.1130/0091-7613(1996)024<0231:CCOTVI>2.3.CO;2.
Masson, D.G., Watts, A.B., Gee, M.J.R., Urgeles, R., Mitchell, N.C., Le Bas, T.P., Canals, M., 2002. Slope failures on the flanks of the western Canary Islands. Earth Sci. Rev. 57 (1–2), 1–35. http://dx.doi.org/10.1016/S0012-8252(01)00069-1.
Masson, D.G., Harbitz, C.B., Wynn, R.B., Pedersen, G., Lovholt, F., 2006. Submarine landslides: processes, triggers and hazard prediction. Phil. Trans. R. Soc. A 364, 2009–2039. http://dx.doi.org/10.1098/rsta.2006.1810.
Masson, D.G., Le Bas, T.P., Grevemeyer, I., Weinrebe, W., 2008. Flank collapse and large-scale landsliding in the Cape Verde Islands, off West Africa. Geochem. Geophys. Geosyst. 9 (7), Q07015. http://dx.doi.org/10.1029/2008GC001983.
Mitchell, N.C., 2001. The transition from circular to stellate forms of submarine volcanoes. J. Geophys. Res. Solid Earth 106 (B2), 1987–2003. http://dx.doi.org/10.1029/2000JB900263.
Mitchell, N.C., 2003. Susceptibility of mid-ocean ridge volcanic islands and seamounts to large-scale landsliding. J. Geophys. Res. 108 (B8), 2397. http://dx.doi.org/10.1029/2002JB001997.
Mitchell, N.C., Masson, D.G., Watts, A.B., Gee, M.J.R., Urgeles, R., 2002. The morphology of the submarine flanks of volcanic ocean islands: a comparative study of the Canary and Hawaiian hotspot islands. J. Volcanol. Geotherm. Res. 115 (1–2), 83–107. http://dx.doi.org/10.1016/S0377-0273(01)00310-9.
Mitchell, N.C., Beier, C., Rosin, P.L., Quartau, R., Tempera, F., 2008. Lava penetrating water: submarine lava flows around the coasts of Pico Island, Azores. Geochem. Geophys. Geosyst. 9 (3), Q03024. http://dx.doi.org/10.1029/2007GC001725.
Mitchell, N.C., Quartau, R., Madeira, J., 2012. Assessing landslide movements in volcanic islands using near-shore marine geophysical data: south Pico Island, Azores. Bull. Volcanol. 74 (2), 483–496. http://dx.doi.org/10.1007/s00445-011-0541-5.
Mitchell, N.C., Quartau, R., Madeira, J., 2013. Large-scale active slump of the southeastern flank of Pico Island, Azores: comment. Geology 41 (12), e301. http://dx.doi.org/10.1130/G34006C.1.
Moore, J.G., Clague, D.A., 2002. Mapping the Nuuanu and Wailau Landslides in Hawaii. In: Takahashi, E., Lipman, P.W., Garcia, M.O., Naka, J., Aramaki, S. (Eds.),Hawaiian volcanoes: deep underwater perspectives. Geophysical Monograph Series, 128. American Geophysical Union, Washington D.C., pp. 223–244. http://dx.doi.org/10.1029/GM128.
Moore, J.G., Clague, D.A., Holcomb, R.T., Lipman, P.W., Normark, W.R., Torresan, M.E., 1989. Prodigious submarine landslides on the Hawaiian Ridge. J. Geophys. Res. Solid Earth 94 (B12), 17465–17484. http://dx.doi.org/10.1029/JB094iB12p17465.
Moore, I.D., Lewis, A., Gallant, J.C., 1993. Terrain properties: estimation methods and scale effects. In: Jakeman, A.J., Beck, M.B., MCaleer, M.J. (Eds.),Modelling Change in Environmental Systems. John Wiley and Sons, New York.
Moore, J.G., Bryan, W.B., Beeson, M.H., Normark, W.R., 1995. Giant blocks in the South Kona landslide, Hawaii. Geology 23 (2), 125–128. http://dx.doi.org/10.1130/0091-7613(1995) 023<0125:GBITSK>2.3.CO;2.
Navarro, J.M., Coello, J., 1989. Depressions Originated by Landslide Processes in Tenerife. ESF Meeting on Canarian Volcanism, Lanzarote 150–152.
Nunes, J.C., 1999. A actividade vulcânica na ilha do Pico do Plistocénico Superior ao Holocénico: Mecanismo eruptivo e hazard vulcânico. PhD thesis Universidade dos Açores, Ponta Delgada, Portugal (356 pp.(available at: http://www.jcnunes.uac.pt/principal.htm)).
Nunes, J.C., 2002. Lateral collapse structures in Pico Island (Azores): mechanism, constraints and age. 3ª Assembleia Luso Espanhola de Geodesia e Geofísica, Valencia, pp. 731–735.
Nunes, J.C., Camacho, A., França, Z., Montesinos, F.G., Alves, M., Vieira, R., Velez, E., Ortiz, E., 2006. Gravity anomalies and crustal signature of volcano-tectonic structures of Pico Island (Azores). J. Volcanol. Geotherm. Res. 156 (1–2), 55–70. http://dx.doi.org/10.1016/j.jvolgeores.2006.03.023.
Quartau, R., Mitchell, N.C., 2013. Comment on "Reconstructing the architectural evolution of volcanic islands from combined K/Ar, morphologic, tectonic, and magnetic data: the Faial Island example (Azores)" by Hildenbrand et al. (2012) [J. Volcanol. Geotherm. Res. 241–242 (2012) 39–48]. Journal of Volcanology and Geothermal Research 255, 124–126. http://dx.doi.org/10.1016/j.jvolgeores.2012.12.020.
Quartau, R., Trenhaile, A.S., Mitchell, N.C., Tempera, F., 2010. Development of volcanic insular shelves: insights from observations and modelling of Faial Island in the Azores Archipelago. Mar. Geol. 275 (1–4), 66–83. http://dx.doi.org/10.1016/j.margeo.2010.04.008.
Quartau, R., Tempera, F., Mitchell, N.C., Pinheiro, L.M., Duarte, H., Brito, P.O., Bates, C.R., Monteiro, J.H., 2012. Morphology of the Faial Island shelf (Azores): the interplay between volcanic, erosional, depositional, tectonic and mass-wasting processes. Geochem. Geophys. Geosyst. 13, Q04012. http://dx.doi.org/10.1029/2011GC003987.
Samper, A., Quidelleur, X., Lahitte, P., Mollex, D., 2007. Timing of effusive volcanism and collapse events within an oceanic arc island: Basse–Terre, Guadeloupe archipelago (Lesser Antilles Arc). Earth Planet. Sci. Lett. 258 (1–2), 175–191. http://dx.doi.org/10.1016/j.epsl.2007.03.030.
Satake, K., Smith, J.R., Shinozaki, K., 2002. Three-dimensional reconstruction and tsunami model of the Nuuanu and Wailau giant landslides, Hawaii. In: Takahashi, E., Lipman, P.W., Garcia, M.O., Naka, J., Aramaki, S. (Eds.),Hawaiian Volcanoes: Deep Underwater Perspectives. Geophysical Monograph Series 128. American Geophysical Union, Washington D.C., pp. 333–346. http://dx.doi.org/10.1029/GM128.
Scheidegger, A.E., 1973. On the prediction of the reach and velocity of catastrophic landslides. Rock Mech. 5 (4), 231–236. http://dx.doi.org/10.1007/BF01301796.
Steiger, R.H., Jäger, E., 1977. Subcommission on geochronology: convention on the use of decay constants in geo- and cosmochronology. Earth Planet. Sci. Lett. 36 (3), 359–362. http://dx.doi.org/10.1016/0012-821X(77)90060-7.
Urgeles, R., Masson, D.G., Canals, M., Watts, A.B., Le Bas, T., 1999. Recurrent large-scale landsliding on the west flank of La Palma, Canary Islands. J. Geophys. Res. Solid Earth 104 (B11), 25331–25348. http://dx.doi.org/10.1029/1999JB900243.
Watts, A.B., Masson, D.G., 2001. New sonar evidence for recent catastrophic collapses of the north flank of Tenerife, Canary Islands. Bull. Volcanol. 63 (1), 8–19.
Woodhall, D., 1974. Geology and volcanic history of Pico Island Volcano, Azores. Nature 248, 663–665. http://dx.doi.org/10.1038/248663a0.